CONTRIBUTIONS TO AUTONOMOUS OPERATION OF A DEEP SPACE VEHICLE POWER SYSTEM

by

Pallavi Kulkarni

A Thesis

Submitted to the Faculty of Purdue University

In Partial Fulfillment of the Requirements for the degree of

Master of Science in Electrical and Computer Engineering

Electrical and Computer Engineering

West Lafayette, Indiana

December 2020

THE PURDUE UNIVERSITY GRADUATE SCHOOL
STATEMENT OF COMMITTEE APPROVAL

Dr. Dionysios Aliprantis, Chair

School of Electrical and Computer Engineering

Dr. Scott Sudhoff

School of Electrical and Computer Engineering

Dr. Ilias Bilionis

School of Mechanical Engineering

Approved by:

Dr. Dimitrios Peroulis

Head of Electrical and Computer Engineering

ACKNOWLEDGMENTS

I am deeply grateful to Prof. Dionysios Aliprantis for his invaluable advice and keen insight that has shaped this thesis. The past two years have been an immense growth process for me because of his mentorship and encouragement to do my best.

I would like to acknowledge National Aeronautics and Space Administration (NASA) for funding this research. I wish to extend special thanks to Jeffrey Csank of NASA Glenn Research Center for giving direction to this work through his regular feedback. I am also thankful to Ning Wu and Benjamin Loop of PC Krause and Associates for their comments and questions in our meetings, that have often helped me inspect the problem more closely.

I would like to thank Prof. Scott Sudhoff and Prof. Ilias Bilionis for serving as my committee members and for their insightful suggestions. In addition, I am glad to have taken some excellent courses by Prof. Sudhoff and Prof. Steven Pekarek, both of whom have always been willing to answer any question I had.

Furthermore, I am grateful to my friends Ayesha Sayed and Harshita Singh for always being there to answer my questions and give me feedback on my work. I also wish to thank all my friends who made this journey memorable.

I am forever grateful to my parents for their constant support and encouragement.

TABLE OF CONTENTS

LIST OF TABLES

LIST OF FIGURES

ABBREVIATIONS

AWG	American Wire Gauge
BCDU	Battery Charge/Discharge Unit
BAT	Battery
CPL	Constant Power Load
DFT	Discrete Fourier Test
FDI	Fault Detection and Identification
IR	Identification Rate
KCL	Kirchhoff's Current Law
KVL	Kirchhoff's Voltage Law
LNR	Largest Normalized Residual
MBSU	Main Bus Switching Unit
MILP	Mixed Integer Linear Program
MM	Mission Manager
MOSFET	Metal Oxide Semiconductor Field Effect Transistor
NASA	National Aeronautics and Space Administration
OPF	Optimal Power Flow
PDU	Power Distribution Unit
PMU	Phasor Measurement Unit
PSA	Parity Space Approach
RBF	Radial Basis Function
RTU	Remote Terminal Unit
SA	Solar Array
SAR	Solar Array Regulator
SC	Short Circuit
SCADA	Supervisory Control and Data Acquisition
SE	State Estimation/Estimator
SVM	Support Vector Machine
WLS	Weighted Least Squares

NOMENCLATURE

$\mathbf{r}$	residual vector
$\mathbf{e}$	vector of error in each measurement
$\mathbf{z}$	chapter 2: vector of measurements
$\mathbf{z}^t$	vector of true values of measured variables
z	chapter 4: state of charge of battery/cell
$\mathbf{x}$	chapter 2: vector of true system states
$\mathbf{x}$	chapter 3: a sample (vector) in feature space
$\mathbf{x}$	chapter 4: vector of variables in the optimization problem
$\hat{\mathbf{x}}$	chapter 2: vector of system state estimates
$\mathbf{x}_u$	chapter 3: an unlabeled sample in feature space
X_k	chapter 3: k-th frequency component of a signal x
$x^{(m)}$	chapter 3: m-th sample in time of signal x
y_u	label of u-th training sample fed to SVM algorithm
I_h^g	measured value of current into load-h connected to PDU-g
V_h^g	measured value of voltage at the terminals of load-h connected to PDU-g
I_m^g	measured value of current from MBSU to PDU-g
V_m^g	measured value of voltage downstream of switch connecting MBSU to PDU-g
I_p^g	measured current into PDU-g sent to the MBSU state estimator
V_p^g	measured voltage of PDU-g central node
$P_{Dh,k}^g$	power demanded by load h connected to PDU-g in time interval-k
$b_{h,k}^g$	status of binary switch of load h connected to PDU-g at k
$c_{h,k}^g$	status of continuous switch of load h connected to PDU-g at k
$W_{h,k}^g$	weight, a measure of importance, of load h connected to PDU-g at k
d_h^g	decision variable that chooses charging profile-h for battery g
$P_{s,r,k}$	line power flow from node-s to node r at k
$P_{s,k}$	power injected into node-s at k
$V_{s,k}$	voltage of bus s at k

ABSTRACT

The electric power system of a deep space vehicle is mission-critical, and needs to operate autonomously because of high latency in communicating with ground-based mission control. Key tasks to be automated include managing loads under various physical constraints, continuously monitoring the system state to detect and locate faults, and efficiently responding to those faults.

This work focuses on three aspects for achieving autonomous, fault-tolerant operation in the dc power system of a spacecraft. First, a sequential procedure is proposed to estimate the node voltages and branch currents in the power system from erroneous sensor measurements. An optimal design for the sensor network is also put forth to enable reliable sensor fault detection and identification. Secondly, a machine-learning based approach that utilizes power-spectrum based features of the current signal is suggested to identify component faults in power electronic converters in the system. Finally, an optimization algorithm is set forth that decides how to operate the power system under both normal and faulted conditions. Operational decisions include shedding loads, switching lines, and controlling battery charging. Results of case studies considering various faults in the system are presented.

1. INTRODUCTION

With increasing integration of renewable energy sources and consumer demand for system reliability, there is a growing interest in intelligent power system operation. Key abilities of such systems include managing loads under various physical constraints, continuously monitoring the system state to detect and locate faults, and efficiently responding to them. These capabilities are particularly important in a critical application like a manned deep space vehicle (DSV), which is the focus of this thesis.

Space vehicles in the low-earth-orbit communicate with ground-based mission control in near real-time. However, for enabling manned missions to venture further, especially beyond cislunar space, the operation of the on-board system must be fully autonomous. This is because the round-trip communication between such a vehicle and ground-control can take several minutes. Hence, if a fault occurs in the power system of such a space vehicle, the on-board system cannot rely on commands from the ground-based control for determining its response. Astronauts on-board are also not expected to have detailed knowledge of each component to make the most effective decisions under different circumstances. Therefore, the on-board system must be capable of operating intelligently under normal conditions as well in response to various faults [1].

First, we analyze the notional architecture of a DSV power system. This analysis reveals certain contrasting features compared to those of a terrestrial power system which has extensively been studied. Specifically, it differs from a terrestrial power system in the way load is forecast, generation is scheduled, and physical states are monitored. The operational objectives also differ, focusing on achieving fault-tolerance rather than on minimizing cost.

1.1 Comparison of DSV power system with terrestrial power system

In terrestrial power systems, several independent consumers demand load depending on their requirement. Generation is scheduled based on the forecast demand, which considers various seasonal and historic factors. A mix of generation sources and energy storage devices often operate in tandem to meet the consumer load demand throughout the day.

However, in the DSV, a computer-based mission manager (MM) determines the desired load schedule that includes individual load demands and their respective priorities for a time horizon encompassing a few hours [2]. Fig. 1.1 shows the power system of a notional deep space vehicle based on the architecture set forth in [3]. In the notional DSV, different power sources cyclically meet the demand of loads connected to each power distribution unit (PDU). Solar arrays SA-1 and SA-2 receive solar energy in a 60 minute-long period of insolation during which they supply power to loads, and charge the batteries on-board. In a subsequent 30 minute-long period of eclipse, the arrays do not generate power. At this time, the batteries are responsible for powering all loads. Batteries and solar arrays are interfaced with the main bus switching units (MBSUs) via power electronic converters (BCDUs and SARs, respectively). The MBSUs that can be tied together by closing switches S_X^1 and S_X^2, which are normally open. The DSV power system is, thus, normally electrically divided in two parts, and the voltage of each MBSU node is regulated to 120 V dc.

Another difference between the two types of systems is in the way their state is monitored. Accurate knowledge of the physical state of the power system is necessary for analyzing power system security and making intelligent decisions related to power dispatch. The problem of estimating the system states such as bus voltages and line currents using the available sensor measurements, which are subject to error, is known as state estimation (SE). In terrestrial grids, various measurements from Remote Terminal Units (RTUs) and Phasor Measurement Units (PMUs) at substations are collated at a Supervisory Control and Data Acquisition (SCADA) system and Phasor Data Concentrator, respectively, and then sent to the control center for this analysis. Several papers address the SE problem for ac power distribution [4], [5] and transmission systems [6]. Weighted least squares (WLS) method is popular for filtering measurement noise in static state estimation [7], [8], whereas Kalman filter-based methods are suggested for dynamic state estimation in a power system [9]–[12]. However, there is limited literature addressing state estimation for dc power systems of critical applications such as space vehicles and future more-electric aircraft [13].

As opposed to PMUs which transmit data 1–2 times per cycle, voltage and current sensors in the DSV transmit measurements at a sampling frequency in the order of hundreds of kHz. The DSV architecture proposed by NASA consists of distributed intelligent

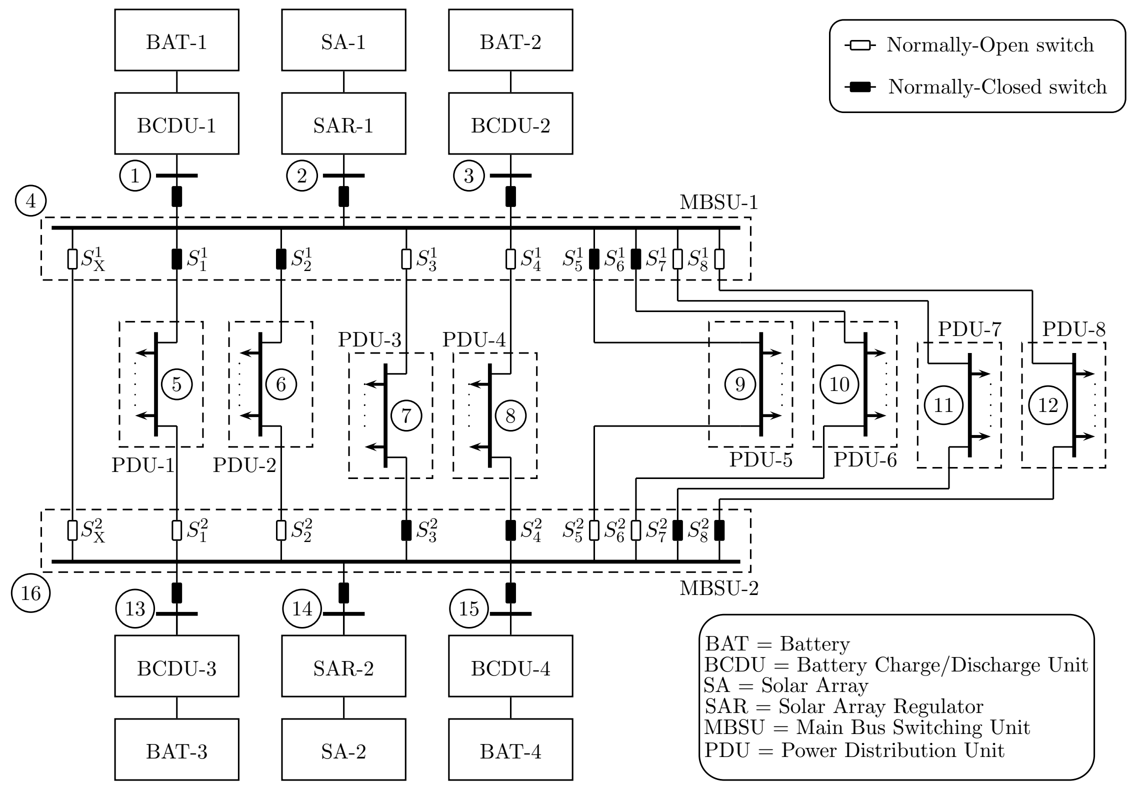

Figure 1.1. Notional deep space power system.

software agents [14], such as microcontrollers, that control each unit such as PDUs and MBSUs. These software agents have access to local measurements and can communicate with other agents. They periodically transmit information to a central controller at a frequency that is a fraction of the sensor sampling frequency.

Given the high sampling frequency, and assuming that control decisions are made based on the observed quasi-steady state and steady state behaviour that the measurements capture, we suggest a WLS-based method to perform static SE. In a centralized SE architecture, measurements from all sensors are aggregated at the central controller. Here, leveraging the features of the distributed software agents, we propose an architecture in which SE is done in parallel by each agent using measurements of local sensors and a subset of sensors from the neighbouring unit. Thus, we solve each SE problem using a subset of measurements used in a centralized scheme. These smaller problems based on WLS can be simplified by making suitable approximations, which gives us insight into the effect of various measurements on the estimates. Using the resulting mathematical equations can speed up the computation of estimates without significant loss of accuracy.

Apart from measurement error due to noise, various sensor faults may compromise the accuracy of the estimates. For instance, incorrect measurements may result from incorrect sensor connection, sensor failure, and cyber-attacks. Several papers address detection of faults in PMUs in terrestrial power systems. Methods to locate such faults are mainly classified as model-based and model-free. Model-free methods that utilize spatio-temporal correlation between measurements of PMUs connected to neighboring nodes have been proposed in [15]–[17]. If there is dissimilarity in the rate of change of measurements by neighbouring sensors due to glitches, a sensor fault is detected. A temporary or constant bias in a sensor is an important sensor fault that needs to be detected and identified. Such a constant offset in measurements by a sensor would not affect this correlation and hence, it could be challenging to identify biased sensors using these methods.

Accuracy of estimates and the ability to detect incorrect sensor measurements depend on the sensor configuration and degree of redundancy of available measurements. Model-based methods can be used as they provide some analytical redundancy through known physical relations that describe the variables being measured. Largest Normalized Residual (LNR) test is a commonly used model-based FDI method, that identifies incorrect measurements based on the difference between measured and estimated quantities. However, it fails under some circumstances when there is low redundancy of sensors.

In [18], conditions are set forth for effective sensor FDI using Parity Space Approach (PSA), another model-based method which has been suggested for electric drives, motors, and electric vehicle applications [19]–[21]. We propose utilizing meaningful relations obtained from the WLS problem that is formulated for SE, that satisfy these conditions. This helps us optimally select additional, practically realizable sensors, which enables us to identify biased sensors. Weight, space requirement, and complexity are constraints in introducing additional sensors in aerospace applications [22]. Hence, a simple design for these additional sensors is put forth, and the volume and weight penalty for this capability is calculated.

Apart from sensor faults, component faults in the dc-dc power electronic converters in the system also need to be identified. Semiconductor devices are particularly fragile [23], so the identification of switch faults has been a main focus [24]–[26]. In model-free methods, a classification system is trained with features computed using measurements of the system under different conditions, which can then be used to predict the system status with new measurements. Prior approaches have relied on neural-networks, support vector machines (SVM), or fuzzy-logic [24]–[29]. Frequency-domain features are commonly used to diagnose faults [30]–[32]. The choice of signal used for FDI is important. In [26], [33], the output voltage was used to generate features that were fed to the proposed FDI algorithm. However, in closed-loop converters with regulated output voltage, this measurement may not reveal enough information for fault diagnosis. A few types of faults were diagnosed in closed-loop converters by model-based techniques proposed in [34], [35] by measuring 2–3 signals.

In this work, we propose an SVM-based method for fault diagnosis in a dc-dc converter system using features related to the power spectrum of a single signal (the input current). The algorithm is tested on a circuit with two back-to-back 3-phase interleaved dc-dc converters. The algorithm returns the fault type, if present, among different types fault types, with high speed and reliability. Normal operating conditions that involve no change or a step change in load are also recognized.

Finally, we can also differentiate between the operational objectives of the two types of power systems. Minimizing cost of electricity and loss [36], [37] are common objectives of electricity market operators of terrestrial grids. Accordingly, an optimization problem known as an optimal power flow (OPF) problem is formulated subject to physical laws and safe operating limits In its simplest form, the OPF problem consists of real variables, such as power injection and voltage at the buses of the network. However, more advanced formulations involving problems like unit commitment [38] and network reconfiguration [39]–[42] also include binary variables.

In this work, our primary objective is ensuring service to important loads and fully charging the batteries. A secondary objective is minimizing network ohmic loss. Accordingly, we define the operational logic of an autonomous control system that ensures optimal system operation under normal and faulted conditions. If a fault occurs in the power system, it is operated in a restorative state. This may involve rerouting power supply to loads by utilizing alternate paths and/or charging batteries at a lower rate. In the proposed algorithm, an OPF problem is formulated as a mixed integer linear program. It is embedded inside an outer loop over all network configurations. The mathematical formulation is relatively simple and computationally efficient.

1.2 Thesis Outline

This work contributes towards three aspects for autonomous, fault-tolerant operation of a power system in a deep space vehicle.

In Chapter 2, a state estimation algorithm is presented which utilizes information from erroneous sensor measurements to estimate voltages and currents throughout the system. Mathematical expressions for the estimates are derived based on WLS method. Based on the insight gained from these expressions, a SE and sensor fault detection algorithm is proposed. A method is also suggested to optimally choose additional sensors to enable detection of faulted current sensors. A simple design for the additional sensors is proposed, based on which the weight penalty for this capability is estimated.

Chapter 3 presents a machine learning approach to accurately and reliably diagnose faults in a dc-dc converter system. The proposed algorithm employs support vector machine (SVM) classification utilizing features related to the power spectrum of the converter input current to identify various component failures.

In Chapter 4, an algorithm is set forth that decides how to operate the system under normal and faulted conditions. Its decisions include shedding loads, switching lines, and controlling battery charging, based on the importance of the loads and the transmission loss. It also decides the network configuration needed to best meet the mission objectives under faulted conditions.

2. STATE ESTIMATION AND BIASED SENSOR IDENTIFICATION

The problem of estimating the physical states of a system using available sensor measurements that may have error is known as state estimation (SE). In this chapter, we derive simple linear expressions to estimate system voltages and currents originating from a Weighted Least Squares (WLS) formulation. The expressions offer insight into the effect of various measurements on the estimates. Using these simple equations for SE is shown to be computationally more efficient than solving the original WLS problem.

In particular, we are interested in detecting current sensor bias. To this end, we propose an approach based on the Largest Normalized Residual (LNR) test. Typically, the ability to detect sensor faults is limited due to sensor cost/weight leading to low sensor redundancy. We propose a method to optimally choose additional sensors and measurements that maximizes our ability to identify the faulted sensor. The proposed SE and sensor fault (bias) detection method is validated using simulation results.

Fig. 2.1 shows a simplified section of the dc power system of the notional deep space vehicle. A dc-dc converter is connected upstream of node-1. The resistance of the circuit connecting the converter to the main bus switching unit (MBSU) is R_c. Here, $n_P = 2$ PDUs are connected to the MBSU with PDU-MBSU circuit resistance R_p. There are n_L constant power loads connected to each power distribution unit (PDU) via switches. The resistance of each switch is R_s.

The system architecture consists of distributed intelligent software agents that controls PDUs and MBSUs [14]. These software agents have access to local measurements, and can communicate with other agents. Utilizing these abilities, SE is performed locally for each unit. The proposed communication architecture in Fig. 2.2 shows the measurements used by the PDU and MBSU agents. Let $\mathbf{V}_P^g$ and $\mathbf{I}_P^g$ be vectors of all voltage and current measurements considered local to PDU-g, respectively, $\forall g \in \{1, \ldots, n_P\}$. Thus,

$$\mathbf{V}_P^g = [V_p^g \quad V_1^g \quad \ldots \quad V_{n_L}^g]\,, \tag{2.1}$$

$$\mathbf{I}_P^g = [I_1^g \quad \ldots \quad I_{n_L}^g]\,. \tag{2.2}$$

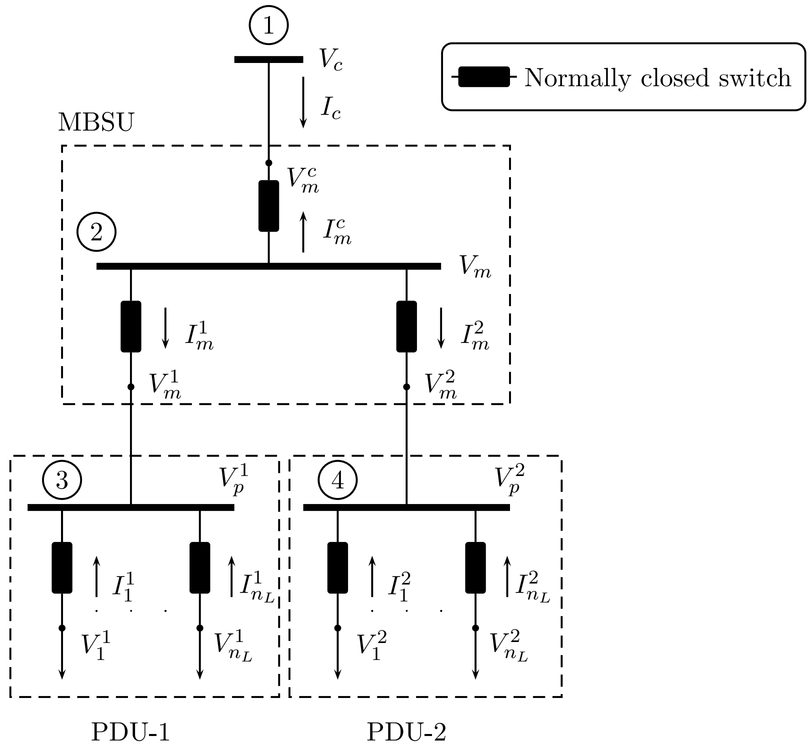

Figure 2.1. Section of deep space vehicle power system.

Let $\mathbf{V}_M$ and $\mathbf{I}_M$ be vectors that include all local MBSU measurements, as well as measurements V_c and I_c from the voltage and current sensor connected to the converter terminal at node-1, respectively. Thus,

$$\mathbf{V}_M = [V_m \quad V_m^1 \quad \dots \quad V_m^{n_P} \quad V_m^c \quad V_c] \,, \tag{2.3}$$

$$\mathbf{I}_M = [I_m^1 \quad \dots \quad I_m^{n_P} \quad I_m^c \quad I_c] \,. \tag{2.4}$$

All voltage and current measurements are assumed to be independent, and have normally-distributed error with zero mean and a standard deviation of σ_v and σ_i, respectively. Based on this architecture and the assumptions mentioned, we propose an SE and biased sensor detection algorithm.

In Section 2.1, we introduce WLS estimation and the LNR test. Next, in Section 2.2, we find approximate expressions for currents and voltages in the PDU and MBSU using

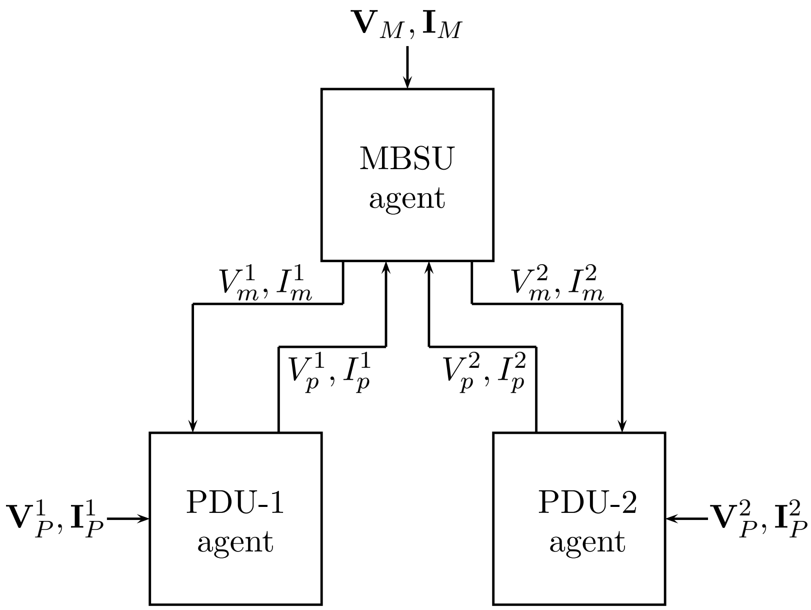

Figure 2.2. Measurements accessed by MBSU and PDU agents.

WLS estimation. From the derived expressions, we deduce that LNR test will not be able to identify faults in PDU current sensors. Hence, in Section 2.4, we propose a method to optimally select additional PDU current sensors. We then derive expressions to estimate the PDU currents using these additional sensor measurements to replace the corresponding expressions found in 2.2. Finally, we present results showing the performance of the proposed SE and sensor fault detection method in Section 2.4.

2.1 Preliminaries

2.1.1 Weighted Least Squares (WLS) estimation

Let $\mathbf{z}$ be an $N_m \times 1$ vector of sensor measurements whose n-th element, z_n, contains the measurement of the n-th sensor. Let $\mathbf{z}^t$ be the corresponding vector of true values of the measured variables. The vector $\mathbf{z}^t$ is linearly related to an $N_s \times 1$ vector of the true system states, $\mathbf{x}$, through an $N_m \times N_s$ matrix $\mathbf{H}$. The unknown error e_n in measurement z_n is independent of the error in all other measurements. We assume that the error has a

Gaussian distribution with zero mean and standard deviation σ_n. Let $\mathbf{e}$ be an $N_m \times 1$ vector of measurement errors. Then, we can express

$$\mathbf{z} = \mathbf{H}\mathbf{x} + \mathbf{e}\,. \tag{2.5}$$

Based on maximum likelihood estimation [7], the objective function can be formulated as

$$\min_{\mathbf{x}} \; J(\mathbf{x}) = \sum_{n=1}^{N_m} \left(\frac{z_n - \mathbf{H}_n \mathbf{x}}{\sigma_n} \right)^2 , \tag{2.6}$$

where $\mathbf{H}_n$ is a $1 \times N_s$ vector (n-th row of $\mathbf{H}$) relating z_n with the states in $\mathbf{x}$. We define a weight matrix

$$\mathbf{W} = \begin{bmatrix} 1/\sigma_1^2 & & & \\ & \cdot & & \\ & & \cdot & \\ & & & 1/\sigma_{N_m}^2 \end{bmatrix} . \tag{2.7}$$

Minimizing $J(\mathbf{x})$ results in the state estimate

$$\hat{\mathbf{x}} = \mathbf{A}^{-1}\mathbf{b}\,, \tag{2.8}$$

where

$$\mathbf{A} = \mathbf{H}^\top \mathbf{W} \mathbf{H}\,, \tag{2.9a}$$

$$\mathbf{b} = \mathbf{H}^\top \mathbf{W} \mathbf{z}\,. \tag{2.9b}$$

Then the measured variables can be estimated as

$$\hat{\mathbf{z}} = \mathbf{H}\hat{\mathbf{x}}\,. \tag{2.10}$$

2.1.2 Largest Normalized Residual (LNR) test

The Largest Normalized Residual (LNR) test is used to detect the presence and identify the source of incorrect measurements based on the difference between the measured and estimated values. A residual vector is defined as

$$\mathbf{r} = \mathbf{z} - \hat{\mathbf{z}} \,. \tag{2.11}$$

From (2.8), (2.9), and (2.10),

$$\mathbf{r} = \mathbf{z} - \mathbf{H}(\mathbf{H}^\top \mathbf{W}\mathbf{H})^{-1}\mathbf{H}^\top \mathbf{W}\mathbf{z} = \mathbf{S}\mathbf{z} \,, \tag{2.12}$$

where the sensitivity matrix

$$\mathbf{S} = \mathbf{I} - \mathbf{H}(\mathbf{H}^\top \mathbf{W}\mathbf{H})^{-1}\mathbf{H}^\top \mathbf{W} \,. \tag{2.13}$$

Note that

$$\mathbf{S}\mathbf{H} = \mathbf{0} \,. \tag{2.14}$$

Hence, from equations (2.5) and (2.12),

$$\mathbf{r} = \mathbf{S}\mathbf{e} \,. \tag{2.15}$$

We can prove that the residual covariance matrix

$$\mathbf{O} = E[\mathbf{r}\mathbf{r}^\top] = \mathbf{S}\mathbf{W}^{-1} \,. \tag{2.16}$$

Incorrect measurements can be detected as follows [7]:

1. Obtain $r_n = z_n - \hat{z}_n, \forall n \in \{1, \ldots, N_m\}$ by performing WLS estimation.

2. Normalize the residuals as

$$r_n^o = r_n / \sqrt{\mathbf{O}_{nn}} \,, \tag{2.17}$$

   which have a standard normal distribution.

3. If $\max(|r_l^o|)$ is greater than a threshold (e.g., 3.0), the l-th measurement is suspected as being corrupted.

The LNR test follows SE to check for faulty sensors. We discuss its implementation in Section 2.3.

2.2 State estimation using approximate expressions

In this section, we derive simple linear expressions to estimate system voltages and currents from a WLS formulation for SE. We analyze the resulting equations, and further propose a simple, alternative method that leads to the same expressions. This alternative method is generalized and can be more computationally efficient than the originally formulated WLS-method.

2.2.1 PDU state estimation using voltages as states

In this section, we derive simplified expressions for estimates of voltages and currents related to the PDU, based on the WLS method.

In the following expressions, we refer to variables related to PDU-g. Hence, for simplicity, we drop the superscript from V_h^g and I_h^g, $\forall h \in \{1, \ldots, n_L\}$. We also denote V_m^g, I_m^g, and V_p^g by V_M, I_M, and V_P, respectively. Here, we solve the WLS problem for $n_L = 2$ considering the PDU local voltages to be states. Thus, let the state estimate vector

$$\hat{\mathbf{x}} = [\hat{V}_P \quad \hat{V}_1 \quad \hat{V}_2]^\top . \tag{2.18}$$

The measurement vector $\mathbf{z}$ includes the local PDU measurements ((2.1) and (2.2)) as well as the measurements sent by the MBSU, as shown in Fig. 2.2. Thus,

$$\mathbf{z} = [V_P \quad V_1 \quad V_2 \quad V_M \quad I_1 \quad I_2 \quad I_M]^\top . \tag{2.19}$$

The currents measured are related to the voltages in the states vector by Kirchhoff's Voltage Law (KVL) and Kirchhoff's Current Law (KCL). Hence, the corresponding matrices for WLS estimation are

$$\mathbf{H} = \begin{bmatrix} 1 & 0 & 0 \\ 0 & 1 & 0 \\ 0 & 0 & 1 \\ 2R_p/R_s + 1 & -R_p/R_s & -R_p/R_s \\ -1/R_s & 1/R_s & 0 \\ -1/R_s & 0 & 1/R_s \\ 2/R_s & -1/R_s & -1/R_s \end{bmatrix}, \tag{2.20}$$

$$\mathbf{W} = \begin{bmatrix} 1/\sigma_v^2 & & & & & & \\ & 1/\sigma_v^2 & & & & & \\ & & 1/\sigma_v^2 & & & & \\ & & & 1/\sigma_v^2 & & & \\ & & & & 1/\sigma_i^2 & & \\ & & & & & 1/\sigma_i^2 & \\ & & & & & & 1/\sigma_i^2 \end{bmatrix}. \tag{2.21}$$

We define the factors

$$\alpha = R_p/R_s \tag{2.22a}$$

$$\gamma = \sigma_v^2/R_s^2\sigma_i^2 \tag{2.22b}$$

From (2.9a), (2.20), and (2.21), we obtain

$$\mathbf{A} = \mathbf{H}^\top\mathbf{W}\mathbf{H} = \frac{1}{\sigma_v^2}\begin{bmatrix} 1 + (2\alpha+1)^2 + 6\gamma & -\alpha(2\alpha+1) - 3\gamma & -\alpha(2\alpha+1) - 3\gamma \\ -\alpha(2\alpha+1) - 3\gamma & 1 + \alpha^2 + 2\gamma & \alpha^2 + \gamma \\ -\alpha(2\alpha+1) - 3\gamma & \alpha^2 + \gamma & 1 + \alpha^2 + 2\gamma \end{bmatrix}. \tag{2.23}$$

Hence, we can find

$$\begin{aligned}\mathrm{Det}(\mathbf{A}) &= \frac{1}{\sigma_v^6}\Big\{[3\gamma^2+\gamma(2\alpha^2+4)+2\alpha^2+1][1+(2\alpha^2+1)^2+6\gamma] \\ &\quad -2[\alpha^2(2\alpha+1)^2+9\gamma^2+6\alpha(2\alpha+1)\gamma](\gamma+1)\Big\} \\ &= \frac{1}{\sigma_v^6}\Big\{9\gamma^2+\gamma^2[3(4\alpha^2+4\alpha+1)+12\alpha^2-24\alpha^2-12\alpha]+\gamma g(\alpha)+f(\alpha)\Big\}\,,\end{aligned} \tag{2.24}$$

where

$$g(\alpha) = -4\alpha^4-8\alpha^3-2\alpha^2-12\alpha+14 \tag{2.25a}$$

$$f(\alpha) = 8\alpha^6+4\alpha^4-8\alpha^3+6\alpha^2+2 \tag{2.25b}$$

Cancelling like terms, this simplifies to

$$\mathrm{Det}(\mathbf{A}) = (12\gamma^2+\gamma g(\alpha)+f(\alpha))/\sigma_v^6\,. \tag{2.26}$$

Manipulating (2.23) and (2.26) to find the inverse of $\mathbf{A}$, we obtain

$$\mathbf{A}^{-1} = \frac{1}{\mathrm{Det}(\mathbf{A})}\begin{bmatrix} a_{11} & a_{12} & a_{13} \\ a_{21} & a_{22} & a_{23} \\ a_{31} & a_{32} & a_{33}\end{bmatrix}\,, \tag{2.27}$$

where

$$a_{11} = [3\gamma^2+2\gamma(\alpha^2+2)+2\alpha^2+1]/\sigma_v^4\,, \tag{2.28a}$$

$$a_{12} = a_{21} = a_{13} = a_{31} = [3\gamma^2+\gamma(2\alpha^2+\alpha+3)+\alpha(2\alpha+1)]/\sigma_v^4\,, \tag{2.28b}$$

$$a_{22} = [3\gamma^2+2\gamma(\alpha^2+\alpha+5)+5\alpha^2+4\alpha+2]/\sigma_v^4\,, \tag{2.28c}$$

$$a_{23} = a_{32} = [3\gamma^2+2\gamma(\alpha^2+\alpha-1)-\alpha^2]/\sigma_v^4\,, \tag{2.28d}$$

$$a_{33} = [3\gamma^2+2\gamma(\alpha^2+\alpha+5)+9\alpha^2+2]/\sigma_v^4\,. \tag{2.28e}$$

From (2.9b), (2.19), (2.20), and (2.21), we obtain

$$\mathbf{b} = \mathbf{H}^\top \mathbf{W}\mathbf{z} = \mathbf{b}_1 - \mathbf{b}_2\,, \tag{2.29}$$

where

$$\mathbf{b}_1 = \frac{1}{\sigma_v^2}\begin{bmatrix} V_P + (2\alpha+1)V_M \\ V_1 - \alpha V_M \\ V_2 - \alpha V_M \end{bmatrix}, \tag{2.30}$$

$$\mathbf{b}_2 = \frac{1}{R_s\sigma_i^2}\begin{bmatrix} I_1 + I_2 - 2I_M \\ I_M - I_1 \\ I_M - I_2 \end{bmatrix}. \tag{2.31}$$

Thus, from (2.8) and (2.29),

$$\hat{\mathbf{x}} = \underbrace{\mathbf{A}^{-1}\mathbf{b}_1}_{\hat{\mathbf{x}}_1} - \underbrace{\mathbf{A}^{-1}\mathbf{b}_2}_{\hat{\mathbf{x}}_2}\,. \tag{2.32}$$

Hence, from (2.27) and (2.30),

$$\hat{\mathbf{x}}_1 = \mathbf{A}^{-1}\mathbf{b}_1 = \frac{1}{\mathrm{Det}(\mathbf{A})}\begin{bmatrix} a_{11} & a_{12} & a_{13} \\ a_{21} & a_{22} & a_{23} \\ a_{31} & a_{32} & a_{33} \end{bmatrix}\frac{1}{\sigma_v^2}\begin{bmatrix} V_P + (2\alpha+1)V_M \\ V_1 - \alpha V_M \\ V_2 - \alpha V_M \end{bmatrix}. \tag{2.33}$$

A cable that can carry the maximum current drawn by the PDU (which is 32 A) for a short distance (of a few meters), considering the desired compactness of a spacecraft has a resistance in the order of mΩ or tens of mΩ. The resistance of commercially available switches that can carry this current is also in the order of mΩ. Hence, their ratio α is of the order of 1 or 10. Also, a much smaller R_s in comparison with σ_v/σ_i results in $\gamma \gg 1$. Then from (2.26),

$$\mathrm{Det}(\mathbf{A}) \approx 12\gamma^2/\sigma_v^6\,. \tag{2.34}$$

Further, while substituting from (2.28) in (2.33), we neglect all terms except the quadratic terms in γ and get

$$\hat{\mathbf{x}}_1 \approx \frac{3\gamma^2}{12\gamma^2}\begin{bmatrix}1 & 1 & 1\\ 1 & 1 & 1\\ 1 & 1 & 1\end{bmatrix}\begin{bmatrix}V_P + (2\alpha+1)V_M\\ V_1 - \alpha V_M\\ V_2 - \alpha V_M\end{bmatrix} = \frac{V_P + V_M + V_1 + V_2}{4}\begin{bmatrix}1\\1\\1\end{bmatrix}. \tag{2.35}$$

Similarly, from (2.27) and (2.31),

$$\hat{\mathbf{x}}_2 = \mathbf{A}^{-1}\mathbf{b}_2 = \frac{\sigma_v^6}{12\gamma^2}\begin{bmatrix}a_{11} & a_{12} & a_{13}\\ a_{21} & a_{22} & a_{23}\\ a_{31} & a_{32} & a_{33}\end{bmatrix}\frac{1}{R_s\sigma_i^2}\begin{bmatrix}I_1 + I_2 - 2I_M\\ I_M - I_1\\ I_M - I_2\end{bmatrix}. \tag{2.36}$$

Substituting (2.28) in (2.36) and considering only the terms involving γ and γ^2 for $\gamma \gg 1$,

$$\begin{aligned}\hat{\mathbf{x}}_2 \approx \frac{R_s}{12\gamma}&\begin{bmatrix}3\gamma^2 + 2\gamma(\alpha^2+2) & 3\gamma^2 + \gamma(2\alpha^2+\alpha+3) & 3\gamma^2 + \gamma(2\alpha^2+\alpha+3)\\ 3\gamma^2 + \gamma(2\alpha^2+\alpha+3) & 3\gamma^2 + 2\gamma(\alpha^2+\alpha+5) & 3\gamma^2 + 2\gamma(\alpha^2+\alpha-1)\\ 3\gamma^2 + \gamma(2\alpha^2+\alpha+3) & 3\gamma^2 + 2\gamma(\alpha^2+\alpha-1) & 3\gamma^2 + 2\gamma(\alpha^2+\alpha+5)\end{bmatrix}\cdot\\ &\begin{bmatrix}I_1 + I_2 - 2I_M\\ I_M - I_1\\ I_M - I_2\end{bmatrix}.\end{aligned} \tag{2.37}$$

Since the rows of $\mathbf{b}_2$ add up to zero, this simplifies to

$$\hat{\mathbf{x}}_2 = \frac{R_s}{12}\begin{bmatrix}4 & \alpha+3 & \alpha+3\\ \alpha+3 & 2(\alpha+5) & 2(\alpha-1)\\ \alpha+3 & 2(\alpha-1) & 2(\alpha+5)\end{bmatrix}\begin{bmatrix}I_1 + I_2 - 2I_M\\ I_M - I_1\\ I_M - I_2\end{bmatrix}. \tag{2.38}$$

This can be rewritten as

$$\hat{\mathbf{x}}_2 = -\frac{I_1R_s}{12}\begin{bmatrix}\alpha-1\\ \alpha+7\\ \alpha-5\end{bmatrix} - \frac{I_2R_s}{12}\begin{bmatrix}\alpha-1\\ \alpha-5\\ \alpha+7\end{bmatrix} + \frac{2I_MR_s}{12}\begin{bmatrix}\alpha-1\\ \alpha+1\\ \alpha+1\end{bmatrix}. \tag{2.39}$$

From (2.32), (2.33), and (2.39),

$$\begin{bmatrix} \hat{V}_P \\ \hat{V}_1 \\ \hat{V}_2 \end{bmatrix} \approx \frac{V_P + V_M + V_1 + V_2}{4} \begin{bmatrix} 1 \\ 1 \\ 1 \end{bmatrix} + \frac{I_1}{12} \begin{bmatrix} R_p - R_s \\ R_p + 7R_s \\ R_p - 5R_s \end{bmatrix} + \frac{I_2}{12} \begin{bmatrix} R_p - R_s \\ R_p - 5R_s \\ R_p + 7R_s \end{bmatrix} - \frac{2I_M}{12} \begin{bmatrix} R_p - R_s \\ R_p + R_s \\ R_p + R_s \end{bmatrix}. \tag{2.40}$$

We can then estimate the current in the loads as follows:

$$\hat{I}_1 = (\hat{V}_1 - \hat{V}_P)/R_s = \frac{2I_1 - I_2 - I_M}{3} = I_1 - \frac{I_1 + I_2 + I_M}{3}, \tag{2.41a}$$

$$\hat{I}_2 = (\hat{V}_2 - \hat{V}_P)/R_s = \frac{2I_2 - I_1 - I_M}{3} = I_2 - \frac{I_1 + I_2 + I_M}{3}. \tag{2.41b}$$

From (2.10) and (2.20),

$$\hat{I}_M = -(\hat{I}_1 + \hat{I}_2) = \frac{2I_M - I_1 - I_2}{3} = I_M - \frac{I_1 + I_2 + I_M}{3}. \tag{2.42}$$

Thus, to estimate each current, a correction term $(I_1 + I_2 + I_M)/3$ is subtracted from the measured value of the corresponding current. The expected value of the correction term is zero, because it is the net current at the PDU bus.

In this way, we find simple linear equations for estimating PDU voltages and currents. The estimates are independent of the standard deviation of the measurement error if $\gamma \gg 1$. Hence, even if the standard deviation of the error is not known exactly, we can estimate the physical circuit variables using simple equations. Because these estimates are a linear combinations of independent measurements, the standard deviation of the estimate can be compared to the standard deviation of its measurement using propagation of uncertainty. For instance, we first rewrite the expression for voltage estimate of $\hat{V}_p$ from (2.40) as

$$\hat{V}_P \approx \frac{V_1 + V_2 + V_M + V_P}{4} + \frac{R_p - R_s}{12}(I_1 + I_2 - 2I_M). \tag{2.43}$$

Then, the standard deviation of the estimate $\hat{V}_p$ can be estimated as

$$\sigma_{\hat{v}_p} = \sqrt{4\sigma_v^2/4^2 + (R_p - R_s)^2(2\sigma_i^2 + 4\sigma_i^2)/12^2}. \tag{2.44}$$

For small resistances, this reduces to

$$\frac{\sigma_{\hat{v}_p}}{\sigma_v} \approx \frac{1}{2} \,. \tag{2.45}$$

Thus, the standard deviation of the voltage estimate is half that of its measurement.

We further wish to construct simple expressions for all voltage and current estimates using a simpler, more general method, for multiple loads connected to a PDU as well as for an MBSU with multiple connected PDUs.

2.2.2 PDU state estimation using current as states

In this subsection, we discuss an alternative approach that considers currents as states to estimate PDU voltages and currents. We show that the derived expressions are the same as found in the previous section. However, this alternative approach helps us to simplify and generalize the method to construct approximate expressions for similar radial networks.

Consider an SE problem in which the state vector

$$\hat{\mathbf{x}} = [\hat{I}_1 \quad \hat{I}_2]^\top \,, \tag{2.46}$$

and the measurement vector

$$\mathbf{z} = [I_1 \quad I_2 \quad I_M]^\top \,. \tag{2.47}$$

Then,

$$\mathbf{H} = \begin{bmatrix} 1 & 0 \\ 0 & 1 \\ -1 & -1 \end{bmatrix} , \tag{2.48}$$

$$\mathbf{W} = \frac{1}{\sigma_i^2} \mathbf{I}_2 \,, \tag{2.49}$$

where $\mathbf{I}_2$ is the 2×2 identity matrix. From (2.9a), (2.48), and (2.49),

$$\mathbf{A} = \mathbf{H}^\top \mathbf{W} \mathbf{H} = \frac{1}{\sigma_i^2} \begin{bmatrix} 2 & 1 \\ 1 & 2 \end{bmatrix} , \tag{2.50}$$

and from (2.9b), (2.48), and (2.49),

$$\mathbf{b} = \mathbf{H}^\top \mathbf{W}\mathbf{z} = \frac{1}{\sigma_i^2} \begin{bmatrix} I_1 - I_M \\ I_2 - I_M \end{bmatrix} . \tag{2.51}$$

Substituting (2.50) and (2.51) in (2.8), we obtain

$$\hat{\mathbf{x}} = \begin{bmatrix} \hat{I}_1 \\ \hat{I}_2 \end{bmatrix} = \begin{bmatrix} I_1 \\ I_2 \end{bmatrix} - \frac{I_1 + I_2 + I_M}{3} \begin{bmatrix} 1 \\ 1 \end{bmatrix} . \tag{2.52}$$

From (2.10) and (2.48),

$$\hat{I}_M = -(\hat{I}_1 + \hat{I}_2) . \tag{2.53}$$

Substituting from (2.52),

$$\hat{I}_M = -(I_1 + I_2) + \frac{2}{3}(I_1 + I_2 + I_M) = I_M - \frac{I_1 + I_2 + I_M}{3} . \tag{2.54}$$

Equations (2.52) and (2.54) match (2.41) and (2.42), respectively. Thus, we obtain the same expressions for current estimates by considering load currents as states and using only current measurements, as we do when voltages are considered states.

Further, we hypothesize that independently calculated current estimates along with voltage measurements can be used to estimate the voltage of the central node in a radial network from the relevant KVL relations of peripheral nodes. Here, the voltage measurements of peripheral nodes are V_1, V_2, and V_M. The estimate of the corresponding branch currents are $\hat{I}_1$, $\hat{I}_2$, and $\hat{I}_M$. We hypothesize that the estimate $\hat{V}_P$ is the average of all KVL relations describing the central node voltage and its own measurement V_P. Thus, if we estimate

$$\hat{V}_P = \frac{1}{4}[V_P + (V_M - R_p \hat{I}_M) + (V_1 - R_s \hat{I}_1) + (V_2 - R_s \hat{I}_2)] , \tag{2.55}$$

we can rewrite it as

$$\hat{V}_P = \frac{V_1 + V_2 + V_M + V_P}{4} - \frac{R_p}{4}\hat{I}_M - \frac{R_s}{4}(\hat{I}_1 + \hat{I}_2) . \tag{2.56}$$

Expanding this equation by substituting (2.52) and (2.54),

$$\hat{V}_P = \frac{V_1 + V_2 + V_M + V_P}{4} + \frac{R_p}{4}\frac{(I_1 + I_2 - 2I_M)}{3} - \frac{R_s}{4}\frac{(I_1 + I_2 - 2I_M)}{3}\,, \tag{2.57}$$

which reduces to

$$\hat{V}_P = \frac{V_1 + V_2 + V_M + V_P}{4} + \frac{R_p - R_s}{12}(I_1 + I_2 - 2I_M)\,. \tag{2.58}$$

This expression matches equation (2.43). Thus, by first performing current estimation and taking the average of terms obtained from relevant KVL equations using the computed current estimates along with voltage measurements, we get the same expression for the estimate of central node voltage as we do when we consider voltages to be states.

We further hypothesize that once the central node voltage is found, we can estimate the voltage of peripheral nodes by applying KVL using the estimated central node voltage and Thus, using (2.55) and (2.52), consider

$$\begin{aligned}
\hat{V}_P + \hat{I}_1 R_s &= \frac{V_1 + V_2 + V_M + V_P}{4} + \frac{R_p - R_s}{12}(I_1 + I_2 - 2I_M) + \frac{R_s}{3}(2I_1 - I_2 - I_M) \\
&= \frac{V_1 + V_2 + V_M + V_p}{4} + \frac{R_p - R_s}{12}(I_1 + I_2 - 2I_M) + \frac{4R_s}{12}(2I_1 - I_2 - I_M) \\
&= \frac{V_1 + V_2 + V_M + V_P}{4} + \frac{R_p}{12}(I_1 + I_2 - 2I_M) + \frac{R_s}{12}(7I_1 - 5I_2 - 2I_M)\,,
\end{aligned} \tag{2.59}$$

which can be rewritten as

$$\hat{V}_P + \hat{I}_1 R_s = \frac{V_1 + V_2 + V_M + V_P}{4} + \frac{I_1}{12}(R_p + 7R_s) + \frac{I_2}{12}(R_p - 5R_s) - \frac{2I_M}{12}(R_p + R_s)\,. \tag{2.60}$$

This expression matches that of $\hat{V}_1$ from (2.40). Thus, we can similarly prove that

$$\hat{V}_g = \hat{V}_P + \hat{I}_g R_s\,, \qquad \forall g \in \{1, 2\}\,. \tag{2.61}$$

We can now draw the following inferences:

1. Current estimation can be treated as an independent problem.

2. The voltage estimate of the central node (here, $\hat{V}_P$) is the average of its prediction obtained by all relevant KVL relations expressed using voltage measurements and current estimates.

3. The voltage of peripheral nodes can be estimated using the voltage estimate of the central node and the corresponding current estimate.

4. If we lose the measurements of a voltage sensor because of a sensor fault or communication failure, we can easily calculate the estimate without having to solve (2.8) using modified matrices. For example, if measurement V_2 becomes unavailable, we can take the average of the other 3 KVL relations, and estimate

$$\hat{V}_P = \frac{1}{3}[V_p + (V_1 - R_s \hat{I}_1) + (V_M - R_p \hat{I}_M)] \,. \tag{2.62}$$

Based on these inferences, we can now generalize the expressions for voltage and current estimates for $n_L \in \mathbb{N}$, $\forall g \in \{1, \ldots, n_P\}$ as follows:

$$\hat{I}_h^g = I_h^g - \frac{1}{n_L + 1}\left(I_m^g + \sum_{l=1}^{n_L} I_l^g\right), \qquad \forall h \in \{1, \ldots, n_L\}\,, \tag{2.63a}$$

$$\hat{I}_p^g = \hat{I}_m^g = -\sum_{h=1}^{n_L} \hat{I}_h^g = I_m^g - \frac{1}{n_L + 1}\left(I_m^g + \sum_{h=1}^{n_L} I_h^g\right), \tag{2.63b}$$

$$\hat{V}_p^g = \frac{1}{n_L + 2}\left[V_p^g + \sum_{h=1}^{n_L}(V_h^g - R_s \hat{I}_h^g) + (V_m^g - R_p \hat{I}_m^g)\right], \tag{2.63c}$$

$$\hat{V}_h^g = \hat{V}_p^g + \hat{I}_h^g R_s \,, \qquad \forall h \in \{1, \ldots, n_L\}\,, \tag{2.63d}$$

$$\hat{V}_m^g = \hat{V}_p^g + \hat{I}_m^g R_p \,. \tag{2.63e}$$

Thus, we can construct generalized approximate expressions for currents and voltages using this alternative approach. The number of arithmetic operations needed to perform SE using these expressions is 2.5–3 times fewer than needed to solve the original WLS problem. In the results section, we compare the accuracy of estimates obtained using these equations with those obtained from the traditional WLS method without making approximations.

2.2.3 MBSU state estimation

Employing the alternative approach described in section 2.2.2, we first perform current estimation of currents local to the MBSU current, and use them to estimate related voltages from appropriate KVL equations.

PDU-g sends measurements V_p^g and $I_p^g = -\sum_{h=1}^{n_L} I_h^g$ to the MBSU. Since measurements I_h^g, $\forall h \in \{1, \ldots, n_L\}$ are independent with standard deviation σ_i, I_p^g would have a standard deviation of $\sqrt{n_L}\sigma_i$. We consider the current flowing from the MBSU to PDUs as states while performing current estimation using WLS method. Thus, let the state estimate vector

$$\hat{\mathbf{x}} = [\hat{I}_m^1 \quad \ldots \quad \hat{I}_m^{n_P}]^\top , \tag{2.64}$$

and the measurement vector

$$\mathbf{z} = [I_p^1 \quad \ldots \quad I_p^{n_P} \quad I_m^1 \quad \ldots \quad I_m^{n_P} \quad I_m^c \quad I_c]^\top . \tag{2.65}$$

Hence,

$$\mathbf{H} = \begin{bmatrix} \mathbf{I}_{n_P} \\ \mathbf{I}_{n_P} \\ -\mathbf{1}_{1\times n_P} \\ \mathbf{1}_{1\times n_P} \end{bmatrix} , \tag{2.66}$$

where $\mathbf{1}_{1\times n_P} = [1 \quad 1 \quad \ldots \quad 1]$, and

$$\mathbf{W} = \frac{1}{\sigma_i^2} \begin{bmatrix} \frac{1}{n_L}\mathbf{I}_{n_P} & & \\ & \mathbf{I}_{n_P} & \\ & & \mathbf{I}_2 \end{bmatrix} . \tag{2.67}$$

First, we solve this problem for $n_P = 2$ PDUs. From (2.9a), (2.66), and (2.67),

$$\mathbf{A} = \mathbf{H}^\top \mathbf{W} \mathbf{H} = \frac{1}{\sigma_i^2} \begin{bmatrix} 3 + 1/n_L & 2 \\ 2 & 3 + 1/n_L \end{bmatrix} . \tag{2.68}$$

Hence, we can find

$$\mathrm{Det}(\mathbf{A}) = \frac{1}{\sigma_i^4}[(3+1/n_L)^2 - 2^2] = \frac{1}{\sigma_i^4}[5+6/n_L+1/n_L^2] = \frac{(n_L+1)(5n_L+1)}{\sigma_i^4 n_L^2}. \tag{2.69}$$

Thus, from (2.68) and (2.69), we find

$$\begin{aligned}\mathbf{A}^{-1} &= \frac{\sigma_i^{-2}}{\mathrm{Det}(\mathbf{A})}\begin{bmatrix} 3+1/n_L & -2 \\ -2 & 3+1/n_L \end{bmatrix} \\ &= \frac{n_L\sigma_i^2}{(n_L+1)(5n_L+1)}\begin{bmatrix} 3n_L+1 & -2n_L \\ -2n_L & 3n_L+1 \end{bmatrix}.\end{aligned} \tag{2.70}$$

From (2.9b), (2.65), (2.66), (2.67),

$$\mathbf{b} = \mathbf{H}^\top\mathbf{W}\mathbf{z} = \frac{1}{n_L\sigma_i^2}\begin{bmatrix} I_p^1 \\ I_p^2 \end{bmatrix} + \frac{1}{\sigma_i^2}\begin{bmatrix} I_m^1 \\ I_m^2 \end{bmatrix} - (I_m^c - I_c)\begin{bmatrix} 1 \\ 1 \end{bmatrix}. \tag{2.71}$$

Thus, from (2.8), (2.70), and (2.71),

$$\begin{aligned}\begin{bmatrix} \hat{I}_m^1 \\ \hat{I}_m^2 \end{bmatrix} = \frac{n_L}{(n_L+1)(5n_L+1)}\Bigg\{&(5n_L+1)\begin{bmatrix} I_m^1 + I_p^1/n_L \\ I_m^2 + I_p^2/n_L \end{bmatrix} - 2n_L\sum_{g=1}^{n_P}(I_m^g + I_p^g/n_L)\begin{bmatrix} 1 \\ 1 \end{bmatrix} \\ &- (n_L+1)(I_m^c - I_c)\begin{bmatrix} 1 \\ 1 \end{bmatrix}\Bigg\}.\end{aligned} \tag{2.72}$$

Similarly, solving for $n_P = 3$ PDUs, from (2.9a), (2.66), and (2.67),

$$\mathbf{A} = \frac{1}{\sigma_i^2}\begin{bmatrix} 3+1/n_L & 2 & 2 \\ 2 & 3+1/n_L & 2 \\ 2 & 2 & 3+1/n_L \end{bmatrix}. \tag{2.73}$$

Hence, we can find

$$
\begin{aligned}
\mathrm{Det}(\mathbf{A}) &= \frac{1}{\sigma_i^6}\{(3+1/n_L)[3+1/n_L)^2-2^2]-4(3+1/n_L-2)+4(-3-1/n_L+2)\} \\
&= \frac{1}{\sigma_i^6}\{(3+1/n_L)[5+6/n_L+1/n_L^2]-8(1+1/n_L)\} \\
&= \frac{1}{\sigma_i^6}\left[\frac{(n_L+1)(3n_L+1)(5n_L+1)}{n_L^3}-\frac{8n_L^2(n_L+1)}{n_L^3}\right] \\
&= \frac{(n_L+1)}{n_L^3\sigma_i^6}(7n_L^2+8n_L+1)\,,
\end{aligned}
\tag{2.74}
$$

which simplifies to

$$
\mathrm{Det}(\mathbf{A}) = \frac{(n_L+1)^2(7n_L+1)}{\sigma_i^6 n_L^3}\,. \tag{2.75}
$$

Thus, from (2.73) and (2.75),

$$
\begin{aligned}
\mathbf{A}^{-1} &= \frac{n_L^3\sigma_i^2}{(n_L+1)^2(7n_L+1)}\begin{bmatrix} 5+6/n_L+1/n_L^2 & -2-2/n_L & -2-2/n_L \\ -2-2/n_L & 5+6/n_L+1/n_L^2 & -2-2/n_L \\ -2-2/n_L & -2-2/n_L & 5+6/n_L+1/n_L^2 \end{bmatrix} \\
&= \frac{n_L\sigma_i^2}{(n_L+1)(7n_L+1)}\begin{bmatrix} 5n_L+1 & -2n_L & -2n_L \\ -2n_L & 5n_L+1 & -2n_L \\ -2n_L & -2n_L & 5n_L+1 \end{bmatrix}.
\end{aligned}
\tag{2.76}
$$

From (2.9b), (2.65), (2.66), and (2.67),

$$
\mathbf{b} = \mathbf{H}^\top\mathbf{W}\mathbf{z} = \frac{1}{n_L\sigma_i^2}\begin{bmatrix} I_p^1 \\ I_p^2 \\ I_p^3 \end{bmatrix} + \frac{1}{\sigma_i^2}\begin{bmatrix} I_m^1 \\ I_m^2 \\ I_m^3 \end{bmatrix} - (I_m^c - I_c)\begin{bmatrix} 1 \\ 1 \\ 1 \end{bmatrix}. \tag{2.77}
$$

Thus, from (2.8), (2.76), and (2.77)

$$\begin{bmatrix} \hat{I}_m^1 \\ \hat{I}_m^2 \\ \hat{I}_m^3 \end{bmatrix} = \frac{n_L}{(n_L+1)(7n_L+1)} \left\{ (7n_L+1) \begin{bmatrix} I_m^1 + I_p^1/n_L \\ I_m^2 + I_p^2/n_L \\ I_m^3 + I_p^3/n_L \end{bmatrix} - 2n_L \sum_{\mathrm{i}=1}^{n_P} (I_m^{\mathrm{i}} + I_p^{\mathrm{i}}/n_L) \begin{bmatrix} 1 \\ 1 \\ 1 \end{bmatrix} \right. \\ \left. - (n_L+1)(I_m^c - I_c) \begin{bmatrix} 1 \\ 1 \\ 1 \end{bmatrix} \right\}. \tag{2.78}$$

As explained in the previous section, current and voltage estimation is done in two successive steps. First, the voltage of the central node in the radial network is estimated. The peripheral node voltage measurements include V_m^c, V_c, V_m^h and V_p^h ,$\forall h \in \{1, \ldots, n_P\}$ The estimates of the corresponding branch currents are $\hat{I}_m^c$, $\hat{I}_c$, $\hat{I}_m^h$ and $\hat{I}_p^h$, $\forall h \in \{1, \ldots, n_P\}$, respectively. The estimate $\hat{V}_m$ is the average of all KVL relations describing the central node voltage and its own measurement V_m. Generalizing, for $n_P \in \mathbb{N}$, $\forall g \in \{1, \ldots, n_P\}$,

$$\hat{I}_m^g = \hat{I}_p^g = \frac{n_L}{n_L+1}(I_m^g + I_p^g/n_L) - \frac{2n_L^2}{(n_L+1)[(2n_P+1)n_L+1]} \sum_{h=1}^{n_P} (I_m^h + I_p^h/n_L) \\ - \frac{n_L}{[(2n_P+1)n_L+1]}(I_m^c - I_c)\,, \tag{2.79a}$$

$$\hat{I}_m^c = -\hat{I}_c = -\sum_{g=1}^{n_P} \hat{I}_m^g\,, \tag{2.79b}$$

$$\hat{V}_m = \frac{1}{2n_P+3} \left\{ V_m + \sum_{h=1}^{n_P} (V_m^h + R_s \hat{I}_m^h) + \sum_{h=1}^{n_P} [V_p^h + (R_s + R_p)\hat{I}_p^h)] \right. \\ \left. + (V_m^c + R_s \hat{I}_m^c) + [V_c - (R_s + R_c)\hat{I}_c] \right\}, \tag{2.79c}$$

$$\hat{V}_m^g = \hat{V}_m - \hat{I}_m^g R_s\,, \tag{2.79d}$$

$$\hat{V}_p^g = \hat{V}_m^g - \hat{I}_p^g R_p\,, \tag{2.79e}$$

$$\hat{V}_m^c = \hat{V}_m - \hat{I}_m^c R_s\,, \tag{2.79f}$$

$$\hat{V}_c = \hat{V}_m^c + \hat{I}_c R_c\,. \tag{2.79g}$$

Thus, general, approximate expressions for MBSU currents and voltages are constructed. In the results section, accuracy of estimates obtained using these equations is compared with those obtained from the traditional WLS method without making approximations.

2.3 Sensor Fault Detection and Identification (FDI)

The WLS method is derived under the assumption that the measurement error has a Gaussian distribution with zero mean. Using the LNR test, we suspect that a measurement is corrupted if the difference between the estimate and the measurement of a variable exceeds the set threshold. This is because, based on the sensor statistics and analytical relationships between the measured variables, such a measurement has low probability of occurrence. This corrupt measurement could be a temporary outlier. If several consecutive measurements in time by a sensor are corrupt, it could indicate the presence of a sensor fault such as a bias.

The concept that the maximum normalized residual corresponds to the corrupt measurement is derived by first assuming that only one sensor (say, sensor-l) has error while others are error-free [7]. Let the l-th sensor error $\mathrm{e}_l \neq 0$, while $\mathrm{e}_n = 0$, $\forall n \in \{1, \ldots, N_m\}$, $n \neq l$. Then, from (2.15), only the l-th column is picked from $\mathbf{S}$, and hence

$$r_n = S_{nl}\, \mathrm{e}_l\,, \qquad \forall n \in \{1, \ldots, N_m\},\, n \neq l\,. \tag{2.80}$$

From (2.15)–(2.17), the normalized residual would be

$$r_n^o = \frac{S_{ln}\mathrm{e}_l}{\sqrt{O_{nn}}} = S_{ln}\mathrm{e}_l\sqrt{\frac{W_{nn}}{S_{nn}}}\,, \qquad \forall n \in \{1, \ldots N_m\}\,. \tag{2.81}$$

Similar to the LNR test, we find the sensor having the maximum normalized residual, and check if it exceeds a predetermined threshold. The threshold $t_n, \forall n \in \{1, \ldots, N_m\}$ is set here as

$$t_n = \mathrm{e}_t\sqrt{S_{nn}W_{nn}}\,, \tag{2.82}$$

where e_t is the error threshold, which we keep fixed for the same type (current/voltage) of sensor. Thus, if $|r_l^o| > |r_n^o|$, $\forall n \in \{1, \ldots, N_m\}\,, n \neq l$, and $|r_l^o| \geq t_l$, sensor-l is suspected as measuring incorrectly. If sensor-l is suspected multiple consecutive times for having large error, we suspect that the sensor has a fault, e.g, a bias. Thus, we use local measurements and a subset of measurements from the neighbouring unit(s) to sequentially perform current and voltage estimation, as explained in section 2.2.2. We test for presence of fault/incorrect measurement in current and voltage sensors after current and voltage estimation, respectively. In both cases, the incorrect sensor measurement can be removed from the measurement vector, and the states re-estimated using the remaining measurements.

2.4 Selection of additional sensors for FDI in PDU current sensors

In this section, we show that the set of current measurements used by the PDU are insufficient for FDI. We then discuss the mathematical foundation that enables FDI in the context of SE using WLS. This helps us determine how current sensors should be chosen for enabling detection of faults in current sensors used for PDU SE. We then present a search algorithm to optimally choose current sensors. With the optimal sensor configuration found, we derive new expressions for PDU current estimates using WLS. We present a simple design for the additional current sensors, based on which we estimate their weight.

From (2.63a) and (2.63b), the residual for the current estimates would be

$$I_h^g - \hat{I}_h^g = I_m^g - \hat{I}_m^g = \frac{1}{n_L + 1}\left(I_m^g + \sum_{l=1}^{n_L} I_l^g\right), \qquad \forall h \in \{1, \ldots, n_L\}. \tag{2.83}$$

Thus, the residuals of all current estimates found by the PDU-SE are equal. If any measurement is incorrect, it will reflect equally in all residuals (2.83). Hence, LNR test fails to identify the faulty sensor in this case. This can also be explained intuitively. Since the only equation relating all the current measurements is the KCL at the central node, if the sum of all current measurements is not zero (or close to zero), it will be impossible to identify which sensor is reading the current incorrectly. Thus, there is a lack of analytical as well as hardware (number of sensors) redundancy in this sensor network. Therefore, to identify faulty sensors amongst PDU current sensors, we propose introducing additional sensors.

2.4.1 Mathematical background to enable FDI

To choose additional sensors that would enable FDI, we use certain relations obtained from SE using WLS.

From (2.14), it follows that rank($\mathbf{S}$) $\geq N_m - N_s$. If the N_s columns of $\mathbf{H}$ are independent, they span the null-space of $\mathbf{S}$, and rank($\mathbf{S}$) $= N_m - N_s$. We will only consider $\mathbf{H}$ matrices that have linearly independent columns. Since $\mathbf{S}$ has $N_m - N_s$ independent columns, its column space is spanned by $N_m - N_s$ eigenvectors corresponding to non-zero eigenvalues. We can also prove that $\mathbf{S}$ is a symmetric matrix. Therefore, the eigenvectors are orthogonal. We will choose these eigenvectors to be orthonormal. Let matrix $\mathbf{Y}$ be an $N_m \times (N_m - N_s)$ matrix whose columns are these orthonormal eigenvectors, which also form the basis of the column space of $\mathbf{S}$. Thus, from (2.15),

$$\mathbf{r} = \mathbf{S}\mathbf{e} = \mathbf{Y}\,\mathbf{r}_P\,, \tag{2.84}$$

where $\mathbf{r}_P$ is an $(N_m - N_s) \times 1$ vector of coefficients, called the parity vector. Since the eigenvectors are orthonormal, we can also express

$$\mathbf{r}_P = \mathbf{Y}^\top\,\mathbf{r}\,, \tag{2.85}$$

Also,

$$\mathbf{Y}^\top\,\mathbf{H} = \mathbf{0}\,. \tag{2.86}$$

So, from (2.85), (2.15), (2.13) and (2.86),

$$\mathbf{r}_P = \mathbf{Y}^\top\mathbf{S}\,\mathbf{e} = \mathbf{Y}^\top\mathbf{e}\,. \tag{2.87}$$

While performing current estimation for a PDU, if we use measurements of only the PDU load currents and the current from the MBSU to the PDU, there would be just $N_m - N_s = 1$ independent eigenvector or axis. The parity vector would have only one component (dimension). Irrespective of which sensor has a large error, only that one component would be affected, in that its magnitude could change. This is another explanation to why it would impossible to identify which of the sensors is faulted.

However, if the $N_m > N_s + 1$, the dimension of the parity vector would be greater than 1. Hence, each of the parity vectors could have distinct directions in multidimensional space. We next show that a biased sensor can be identified if each parity vector has a distinct direction in such a space.

Consider, for instance, a case where $N_m - N_s = 3$, resulting in a 3D-parity space. Let the w-th eigenvector/axis

$$\mathbf{Y}_w = [y_1^w \ \dots \ y_{N_m}^w]^\top , \qquad w \in \{1, 2, 3\} . \tag{2.88}$$

If there is unit error only in the l-th sensor, with no noise in the measurements, the l-th element of $\mathbf{e}$ would be unity, while the other elements would be zero. Thus, from (2.87), the parity vector, denoted by $\mathbf{r}_\mathrm{e}^l$, would pick up the l-th column from $\mathbf{Y}^\top$ (l-th row of $\mathbf{Y}$, having dimension $N_m - N_s$). Thus,

$$\mathbf{r}_\mathrm{e}^l = [y_l^1 \quad y_l^2 \quad y_l^3]^\top \tag{2.89}$$

If there is a large error in sensor-l equal to e_l, with no noise in other measurements, the parity vector would be

$$\mathbf{r}_P = \mathrm{e}_l \, [y_l^1 \quad y_l^2 \quad y_l^3]^\top \tag{2.90}$$

Practically, there may be some error (smaller in magnitude compared to e_l) due to noise in the other measurements. Thus, the parity vector would have elements that are close to $(\mathrm{e}_l y_l^1, \mathrm{e}_l y_l^2, \mathrm{e}_l y_l^3)$ but may not be exactly as defined in (2.90). This implies that for a large positive error, $\mathbf{r}_P$ will lie close to the ray in the direction of $\mathbf{r}_\mathrm{e}^l$, whereas for a large negative error, $\mathbf{r}_P$ will lie close to the ray in the direction of $-\mathbf{r}_\mathrm{e}^l$. The vectors $\mathbf{r}_\mathrm{e}^l$ and $-\mathbf{r}_\mathrm{e}^l$, $\forall l \in \{1, \dots, N_m\}$, are henceforth referred to as error-rays. From (2.90), the length of the parity vector $\mathbf{r}_P$ increases with increase in magnitude of e_l. If all the error-rays are distinct, a bias in each sensor will result in a distinct parity vector in the corresponding error-ray direction. This will enable FDI in the sensors.

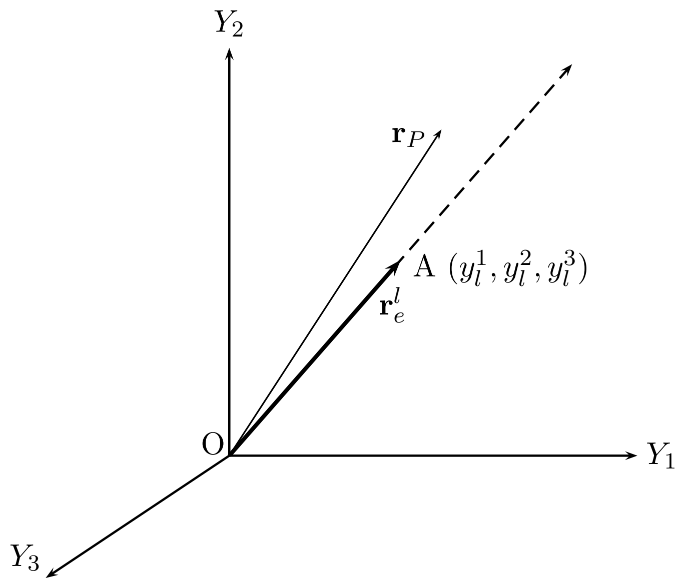

Figure 2.3. Parity vector due to error in sensor-l in parity-space.

The mathematical properties discussed in this section form the foundation for selection of additional sensors, which is discussed in the next section.

2.4.2 Search algorithm for additional optimal sensors

The objective is to find a set of measurements of combinations of load currents (as defined by a matrix $\mathbf{H}$) that can best distinguish between faults in various sensors.

From (2.89), if $\mathbf{r}_\mathrm{e}^l$ has a much smaller magnitude compared to $\mathbf{r}_\mathrm{e}^n$, $\forall n \in \{1, \ldots, N_m\}$, $n \neq l$, the parity vector of an extra noisy measurement or outlier, whose direction is close that of $\mathbf{r}_\mathrm{e}^l$ could be mistaken to be the result of a large error in sensor-l. This implies that the magnitudes of all $\mathbf{r}_\mathrm{e}^n$, $\forall n \in \{1, \ldots, N_m\}$, (e.g., length of segment $\overline{\mathrm{OA}}$ in Fig. 2.3), should be large and close in length. Also, for effective discrimination between faults in various sensors, the rays need to be well-separated in the parity-space.

Consider all possible $\mathbf{H}$ matrices of the form

$$\mathbf{H} = \begin{bmatrix} \mathbf{I}_{n_L} \\ \mathbf{C} \\ -\mathbf{1}_{1\times n_L} \end{bmatrix}, \tag{2.91}$$

where $\mathbf{C}$ is an $c_n \times N_s$ matrix $c_n \in \mathbb{N}$. Thus, the first n_L sensors measure load currents. The next c_n sensors measures some combination of at least c_n load currents with the constraint that elements of $\mathbf{C} \in \{-1, 0, 1\}$, for simplicity of sensor design. The last sensor, local to the MBSU, measures the current flowing into the PDU. Such combination of measurements leads to an $\mathbf{H}$ matrix that has linearly independent columns.

We perform a brute force search over all N_c possible $\mathbf{H}$ matrices, $\mathbf{H}_n$, $\forall n \in \{1, \ldots, N_c\}$, with $n_c = 1$ for the optimal matrix according to the algorithm in Fig. 2.4. Let q be the the ratio of magnitude of the shortest error-ray to the length of the longest error-ray. The matrices leading to error-ray that are relatively close in magnitude (checked by q) are short-listed. We then normalize each error-ray to length. The product of distance of every tip of normalized error-ray from every other is defined here as the separation. The $\mathbf{H}$ matrix leading to the best separated rays is chosen. If no matrix satisfies these conditions, we repeat the brute force algorithm with $n_c = 2$, and so on.

Let $\mathbf{X}$ be an $n_L \times n_L$ matrix of ones. Thus,

$$\mathbf{X}_{n_L} = \begin{bmatrix} 1 & \cdot & \cdot & 1 \\ \cdot & \cdot & \cdot & \cdot \\ \cdot & \cdot & \cdot & \cdot \\ 1 & \cdot & \cdot & 1 \end{bmatrix}. \tag{2.92}$$

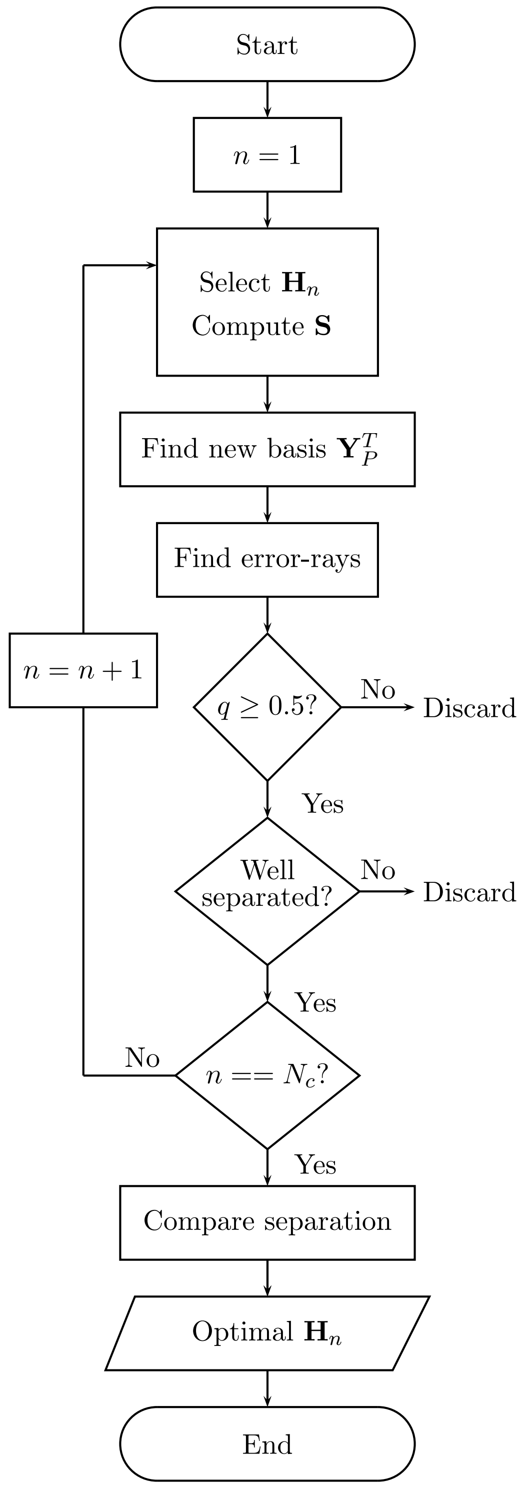

Figure 2.4. Brute-force search for optimal measured combinations.

Performing the search according to the algorithm, the shortlisted matrices were found to have the following properties:

$$\mathbf{C}\mathbf{C}^\top = 6\,\mathbf{I}_2\,, \tag{2.93a}$$

$$\mathbf{C}\mathbf{X} = \mathbf{0}_{2\times n_L}\,, \tag{2.93b}$$

$$\mathbf{X}\mathbf{C}^\top = \mathbf{0}_{n_L\times 2}\,, \tag{2.93c}$$

These properties will be used in the next section to simplify the expression for PDU current estimate. The matrix determined to be optimal for $n_L = 8$

$$\mathbf{C} = \begin{bmatrix} -1 & 0 & -1 & 0 & 1 & 1 & 1 & -1 \\ 1 & 1 & -1 & -1 & 0 & -1 & 1 & 0 \end{bmatrix}. \tag{2.94}$$

Thus, 2 additional sensors are chosen that measure a combination of 6 load currents.

2.4.3 PDU state estimation using additional sensors

In this section, we derive PDU current estimates, with the additional measurements included, using WLS. With the chosen additional measurements, denoted as I_{A1} and I_{A2} corresponding to rows n_L+1 and n_L+2 of (2.91), the state estimate vector for PDU-g, $\forall g \in \{1,\dots n_P\}$ for current estimation is still

$$\hat{\mathbf{x}} = [\hat{I}_1^g \quad \dots \quad \hat{I}_{n_L}^g]^\top, \tag{2.95}$$

while the measurement vector changes to

$$\mathbf{z} = [\,\underbrace{I_1^g \quad \dots \quad I_{n_L}^g}_{\mathbf{I}_L^g} \quad \underbrace{I_{A1}^g \quad I_{A2}^g}_{\mathbf{I}_A^g} \quad I_m^g]^\top, \tag{2.96}$$

where $\mathbf{I}_L^g$ and $\mathbf{I}_A^g$ are column vectors. The measurement vector $\mathbf{I}_P^g$ from (2.2) thus changes to

$$\mathbf{I}_P^g = \begin{bmatrix} \mathbf{I}_L^g \\ \mathbf{I}_A^g \\ I_m^g \end{bmatrix}^\top . \tag{2.97}$$

Assuming the additional sensors have similar error statistics as the other current sensors, the weight matrix

$$\mathbf{W} = \frac{1}{\sigma_{\mathrm{i}}^2}\mathbf{I}_{(n_L+3)} . \tag{2.98}$$

From (2.9a),

$$\mathbf{A} = \mathbf{H}^\top \mathbf{W}\mathbf{H} = \frac{1}{\sigma_i^2}\mathbf{H}^\top \mathbf{H} . \tag{2.99}$$

From (2.91),

$$\mathbf{H}^\top \mathbf{H} = \begin{bmatrix} \mathbf{I}_{n_L} & \mathbf{C}^\top & -\mathbf{1}_{n_L \times 1} \end{bmatrix} \cdot \begin{bmatrix} \mathbf{I}_{n_L} \\ \mathbf{C} \\ -\mathbf{1}_{1\times n_L} \end{bmatrix} = \mathbf{I}_{n_L} + \mathbf{C}^\top \mathbf{C} + \mathbf{X}_{n_L} = \underbrace{(\mathbf{I}_{n_L} + \mathbf{X})}_{\mathbf{P}} + \mathbf{C}^\top \mathbf{C} . \tag{2.100}$$

Thus, from (2.99) and (2.100),

$$\mathbf{A} = \frac{1}{\sigma_i^2}(\mathbf{P} + \mathbf{C}^\top \mathbf{C}) . \tag{2.101}$$

For WLS estimation, we will require $\mathbf{A}^{-1}$, which can be found by

$$\mathbf{A}^{-1} = \sigma_i^2 (\mathbf{P} + \mathbf{C}^\top \mathbf{C})^{-1} . \tag{2.102}$$

The matrix $\mathbf{P} = \mathbf{I} + \mathbf{X}$ is a full-rank matrix. Thus its inverse exists, and hence, we can apply the Woodbury matrix identity to expand the above equation. According to the Woodbury matrix identity,

$$(\mathbf{B} + \mathbf{D}\mathbf{Q}\mathbf{R})^{-1} = \mathbf{B}^{-1} - \mathbf{B}^{-1}\mathbf{D}(\mathbf{Q}^{-1} + \mathbf{R}\mathbf{B}^{-1}\mathbf{D})^{-1}\mathbf{V}\mathbf{B}^{-1} , \tag{2.103}$$

where $\mathbf{B}$, $\mathbf{D}$, $\mathbf{Q}$, and $\mathbf{R}$ are $n \times n$, $n \times l$, $l \times l$, and $l \times n$ matrices, respectively. Putting $\mathbf{B} = \mathbf{P}$, $\mathbf{D} = \mathbf{C}^\top$, $\mathbf{Q} = \mathbf{I}_2$, and $\mathbf{R} = \mathbf{C}$, we get

$$(\mathbf{P} + \mathbf{C}^\top \mathbf{I_2} \mathbf{C})^{-1} = \mathbf{P}^{-1} - \mathbf{P}^{-1}\mathbf{C}^\top (\mathbf{I}_2 + \mathbf{C}\mathbf{P}^{-1}\mathbf{C}^\top)^{-1} \mathbf{C}\mathbf{P}^{-1}\,. \tag{2.104}$$

The inverse of $\mathbf{P}$ can be found as

$$\mathbf{P}^{-1} = (\mathbf{I}_{n_L} + \mathbf{X})^{-1} = \begin{bmatrix} 2 & 1 & \cdot & 1 \\ 1 & 2 & \cdot & 1 \\ \cdot & \cdot & \cdot & \cdot \\ 1 & 1 & \cdot & 2 \end{bmatrix}^{-1} = \frac{1}{n_L + 1} \begin{bmatrix} n_L & -1 & \cdot & -1 \\ -1 & n_L & \cdot & -1 \\ \cdot & \cdot & \cdot & \cdot \\ -1 & -1 & \cdot & n_L \end{bmatrix}. \tag{2.105}$$

Thus, we can express

$$\mathbf{P}^{-1} = \frac{1}{n_L + 1}[\,(n_L + 1)\mathbf{I}_{n_L} - \mathbf{X}\,] = \mathbf{I}_{n_L} - \frac{1}{n_L + 1}\mathbf{X}\,. \tag{2.106}$$

Equation (2.104) can be rewritten as

$$(\mathbf{P} + \mathbf{C}^\top \mathbf{C})^{-1} = \mathbf{P}^{-1}\left[\mathbf{I}_{n_L} - \mathbf{C}^\top (\mathbf{I}_2 + \underbrace{\mathbf{C}\mathbf{P}^{-1}\mathbf{C}^\top}_{\mathbf{P}_c})^{-1} \mathbf{C}\mathbf{P}^{-1}\right]. \tag{2.107}$$

Substituting from (2.106),

$$\mathbf{P}_c = \mathbf{C}\mathbf{P}^{-1}\mathbf{C}^\top = \mathbf{C}\left(\mathbf{I}_{n_L} - \frac{1}{n_L + 1}\mathbf{X}\right)\mathbf{C}^\top = \mathbf{C}\mathbf{C}^\top - \frac{1}{n_L + 1}\mathbf{C}\mathbf{X}\mathbf{C}^\top\,. \tag{2.108}$$

Thus, from (2.93a) and (2.93c),

$$\mathbf{P}_c = \mathbf{C}\mathbf{C}^\top = 6\,\mathbf{I}_2\,. \tag{2.109}$$

Plugging this result into (2.107),

$$\begin{aligned} (\mathbf{P} + \mathbf{C}^\top \mathbf{C})^{-1} &= \mathbf{P}^{-1}\left[\mathbf{I}_{n_L} - \mathbf{C}^\top (7\,\mathbf{I}_2)^{-1} \mathbf{C}\mathbf{P}^{-1}\right] \\ &= \mathbf{P}^{-1}\left[\mathbf{I}_{n_L} - \frac{1}{7}\mathbf{C}^\top \mathbf{C}\mathbf{P}^{-1}\right]. \end{aligned} \tag{2.110}$$

Expanding (2.110) using (2.106), and then simplifying using (2.93b),

$$\begin{aligned}(\mathbf{P}+\mathbf{C}^\top\mathbf{C})^{-1} &= \Big(\mathbf{I}_{n_L} - \frac{1}{n_L+1}\mathbf{X}\Big)\Big[\mathbf{I}_{n_L} - \frac{1}{7}\mathbf{C}^\top\mathbf{C}\Big(\mathbf{I}_{n_L} - \frac{1}{n_L+1}\mathbf{X}\Big)\Big] \\ &= \Big(\mathbf{I}_{n_L} - \frac{1}{n_L+1}\mathbf{X}\Big)\Big[\mathbf{I}_{n_L} - \frac{1}{7}\mathbf{C}^\top\mathbf{C}\Big]\end{aligned}. \tag{2.111}$$

Using (2.93c),

$$(\mathbf{P}+\mathbf{C}^\top\mathbf{C})^{-1} = \mathbf{I}_{n_L} - \frac{1}{n_L+1}\mathbf{X} - \frac{1}{7}\mathbf{C}^\top\mathbf{C}\,. \tag{2.112}$$

Plugging this result into (2.101),

$$\mathbf{A}^{-1} = \sigma_i^2\Big(\mathbf{I}_{n_L} - \frac{1}{n_L+1}\mathbf{X} - \frac{1}{7}\mathbf{C}^\top\mathbf{C}\Big)\,. \tag{2.113}$$

Substituting from (2.9b), (2.113), (2.98), and (2.91) in (2.8), and dropping the dimension subscripts, we get

$$\begin{aligned}\hat{\mathbf{x}} &= \mathbf{A}^{-1}\mathbf{H}^\top\mathbf{W}\mathbf{z} \\ &= \sigma_i^2\left(\mathbf{I} - \frac{1}{n_L+1}\mathbf{X} - \frac{1}{7}\mathbf{C}^\top\mathbf{C}\right)\begin{bmatrix}\mathbf{I} & \mathbf{C}^\top & -\mathbf{1}\end{bmatrix}\frac{1}{\sigma_i^2}\mathbf{I}\,\mathbf{z}\,.\end{aligned} \tag{2.114}$$

Expanding it, and then using (2.93a) and (2.93c),

$$\begin{aligned}\hat{\mathbf{x}} &= \begin{bmatrix}\mathbf{I} - \tfrac{1}{n_L+1}\mathbf{X} - \tfrac{1}{7}\mathbf{C}^\top\mathbf{C} & \mathbf{C}^\top - \tfrac{1}{n_L+1}\mathbf{X}\mathbf{C}^\top - \tfrac{1}{7}\mathbf{C}^\top\mathbf{C}\mathbf{C}^\top & -(1-\tfrac{n_L}{n_L+1})\mathbf{1} + \tfrac{1}{7}\mathbf{C}^\top\mathbf{C}\mathbf{1}\end{bmatrix}\mathbf{z} \\ &= \begin{bmatrix}\mathbf{I} - \tfrac{1}{n_L+1}\mathbf{X} - \tfrac{1}{7}\mathbf{C}^\top\mathbf{C} & \tfrac{1}{7}\mathbf{C}^\top & -\tfrac{1}{n_L+1}\mathbf{1}\end{bmatrix}\mathbf{z}\end{aligned}. \tag{2.115}$$

Substituting from (2.96), the vector of load current estimates for PDU-g,

$$\hat{\mathbf{I}}_L^g = \mathbf{I}_L^g - \frac{1}{n_L+1}\left(\sum_{h=1}^{n_L} I_h^g + I_m^g\right)\mathbf{1}_{n_L\times 1} - \frac{1}{7}\mathbf{C}^\top(\,\mathbf{C}\mathbf{I}_L^g - \mathbf{I}_A^g)\,. \tag{2.116}$$

The vector of estimates for the 2 additional sensors can be found by

$$\hat{\mathbf{I}}_A^g = \mathbf{C}\hat{\mathbf{I}}_L^g\,. \tag{2.117}$$

The current from the MBSU to the PDU can be estimated as

$$\hat{I}^g_m = -\sum_{h=1}^{n_L} \hat{I}^g_h \,. \tag{2.118}$$

Note that the residual of the load current estimates would be

$$\mathbf{I}^g_L - \hat{\mathbf{I}}^g_L = \frac{1}{n_L+1}\left(\sum_{h=1}^{n_L} I^g_h + I^g_m\right)\mathbf{1}_{n_L\times 1} + \frac{1}{7}\mathbf{C}^\top(\,\mathbf{C}\mathbf{I}^g_L - \mathbf{I}^g_A)\,. \tag{2.119}$$

Comparing (2.119) with (2.83), the additional term is $\frac{1}{7}\mathbf{C}^\top(\,\mathbf{C}\mathbf{I}^g_L - \mathbf{I}^g_A)$. The properties (2.93) make it possible to derive this expression.

Expressions (2.116)–(2.117) can be used for current estimation, and will not require matrix inversion or other algorithms used for solving a set of linear equations. They replace (2.63a)–(2.63b). Then, the LNR test is performed for current sensor FDI; currents can be re-estimated by removing the suspected measurements if bias is detected. Following that, voltage estimation is performed according to (2.63c)–(2.63e) using voltage measurements and the estimated currents. Finally, voltage sensors are tested for faults. If present, the voltages are re-estimated after removing the suspected measurements.

2.4.4 Sensor design

In this section, we design a sensor that relies on the Hall Effect for measuring each of the additional PDU quantities I_{A1} and I_{A2}.

The Hall Effect is observed in the presence of a magnetic field perpendicular to the direction of current flow in a conductor or semiconductor known as the Hall element. When such a magnetic field is applied to the Hall element, its charge carriers experience the Lorentz force. The resulting distribution of current density establishes an electric field across the conductor, perpendicular to the direction of current and to the magnetic field. This effect is utilized by a Hall effect sensor. Such a sensor measures the voltage produced across the Hall element, to find the magnitude of the applied magnetic field, which is proportional to the voltage [43]. If this magnetic field is set up by a current, or in our case, a combination of currents, we can find its magnitude using such a sensor.

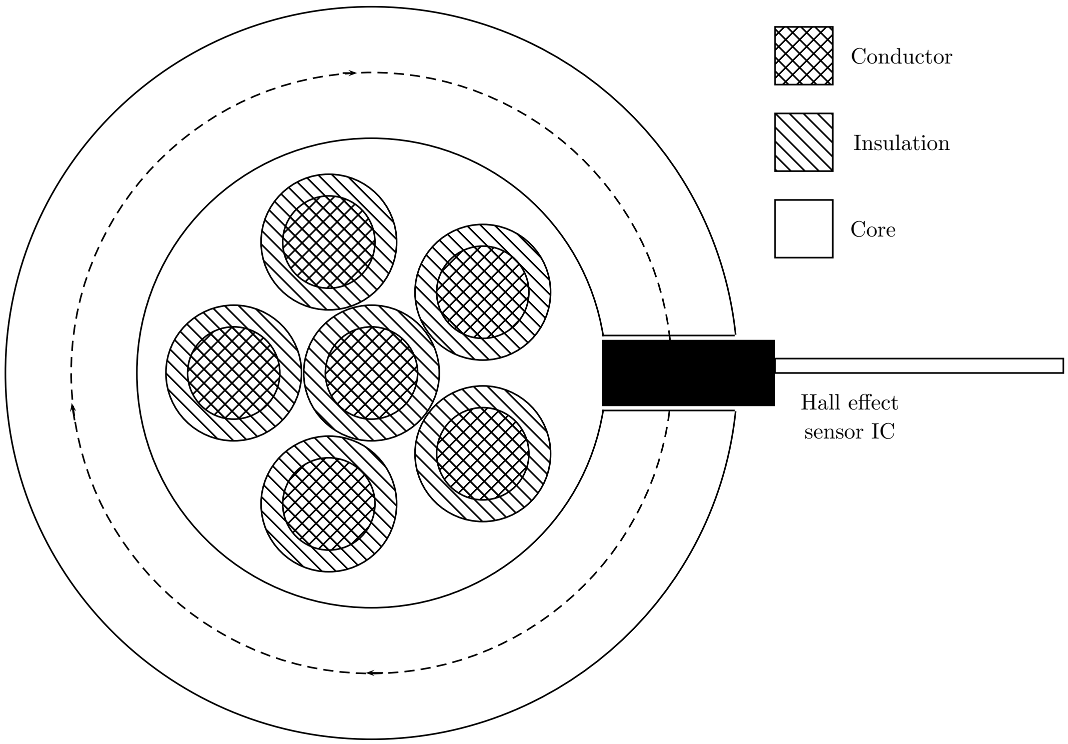

Figure 2.5. Cross-sectional view of proposed additional sensor.

We select conductor of AWG 14 whose ampacity is 32 A, and diameter is 1.628 mm for carrying the load current. With the appropriate PVC insulation of thickness (0.381 mm), the outer diameter of the cable would be $1.628 + 2 \times 0.381 \approx 2.39$ mm. To fit 6 such cables, a toroid with an inner diameter $d_i = 8.14$ mm, outer diameter $d_o = 12.7$ mm, and height $h = 3.18$ mm is selected. The material-L with a relative permeability $\mu_r = 900$ is chosen [44].

Hall Effect sensor IC EQ731L [45] can measure up to ±38.5 mT. Since its width is 1.15 mm, let the air gap g be 1.3 mm to allow for some clearance between the core and the IC. The cross-section of the proposed sensor is shown in Fig. 2.5. The mean path length l for the flux inside the core is

$$l = \frac{(2\pi - \theta)}{2\pi} \frac{\pi(d_i + d_o)}{2}, \tag{2.120}$$

where

$$\theta = 2\arcsin\left[2g/(d_i + d_o)\right]. \tag{2.121}$$

Let B be the magnetic flux density and A be the area of the flux path inside the core. Then, the reluctances of the air gap and the core are $R_g = g/(\mu_0 A)$ and $R_c = l/(\mu_0 \mu_r A)$, respectively, where μ_0 is the permeability of free space. Then the magnetic flux

$$\Phi = BA = \frac{\sum_{n=1}^{6} N_n I_n}{R_g + R_c} = \frac{\mu_0 \mu_r A \sum_{n=1}^{6} N_n I_n}{\mu_r g + l}. \tag{2.122}$$

where N_n is the number of turns of the n-th conductor enclosed by the flux path carrying current I_n. Since $N_1 = \ldots = N_6 = 1$,

$$B = \frac{\mu_0 \mu_r \sum_{n=1}^{6} I_n}{\mu_r g + l}. \tag{2.123}$$

For a maximum load demand of 4 A, the maximum magnitude of the sum of currents is 12 A (from (2.94)). Substituting this in (2.123), the maximum magnitude of $B = 11.3$ mT, which is within the range of the flux density that the Hall Effect sensor can measure.

The core material has a density $\rho = 4.8$ g/cm^3. So, the weight of the toroid would be $\rho\left[\frac{\pi(d_o^2 - d_i^2)}{4} - \frac{g(d_o - d_i)}{2}\right]h = 1.09$ g. Hence, the total weight of the toroids of the 2 extra sensors is 2.18 g.

Thus, the weight and space requirement based on a simple design for the additional sensors that lend FDI capability to the PDU-SE is calculated.

2.5 Results

In this section, we present simulation based results that statistically show the performance of the SE and bias detection algorithm.

The system considered has $n_P = 2$ PDUs connected to an MBSU, with $n_L = 8$ loads connected to each PDU. The resistances $R_s = 3$ mΩ, $R_p = 8$ mΩ, and $R_c = 4$ mΩ. For a fixed operating point of $V_m = 120$ V, and load currents as given in Table 2.1, $R = 2000$

Table 2.1. Current drawn by each load

Load no.	PDU-1	PDU-1
1	3.73 A	3.68 A
2	1.77 A	2.16 A
3	3.67 A	1.11 A
4	2.72 A	1.84 A
5	2.61 A	2.05 A
6	1.02 A	2.29 A
7	3.56 A	2.73 A
8	2.11 A	0.15 A

measurements of each circuit variable with random normally-distributed error are taken. For all voltage and current measurements, the standard deviation of the error is $\sigma_v = 0.1$ V and $\sigma_i = 0.2$ A, respectively.

Let z^t be the true value of some variable, and z_r be its measurement in the r-th set of measurements. The MBSU estimates are obtained from (2.79). PDU currents are estimated using (2.116), (2.117)–(2.118), while its voltages are estimated using (2.63c)–(2.63e). Let the estimate corresponding to z_r be $\hat{z}_r$. The sample mean of the estimate $\hat{z}_r$ over all R sets

$$\mu_z = \frac{1}{R}\sum_{r=1}^{R} \hat{z}_r \,, \tag{2.124}$$

while its standard deviation

$$\sigma_z = \sqrt{\frac{1}{R-1}\sum_{r=1}^{R} \left(\hat{z}_r - \mu_z\right)^2} \,. \tag{2.125}$$

The % difference between the mean estimate and the true value of the measured quantity is calculated as

$$d_z = \frac{|\mu_z - z^t|}{|z^t|} \times 100 \,. \tag{2.126}$$

These metrics will be used to evaluate the accuracy of various estimates based on the derived approximate expressions.

Table 2.2. Accuracy comparison

Variables	WLS method		Proposed method		Calculated
	$d_z(\%)$	σ_z	$d_z(\%)$	σ_z	σ
PDU voltages	1.5×10^{-4}	32.1 mV	$2.0\ \times10^{-4}$	30.6 mV	31.7 mV
PDU currents	6.4×10^{-2}	164.0 mA	17.1×10^{-2}	163.6 mA	164.0 mA
MBSU voltages	3.0×10^{-4}	37.8 mV	6.2×10^{-4}	37.9 mV	37.8 mV
MBSU to PDU currents	8.1×10^{-3}	146.5 mA	3.1×10^{-2}	144.3 mA	145.7 mA
Converter to MBSU current	4.3×10^{-3}	125.9 mA	1.5×10^{-3}	124.6 mA	123.7 mA

2.5.1 Validation of analytical expressions for state estimation

In this section, we compare the performance of the SE method using the derived approximate expressions with the method using WLS formulation. To solve the WLS problem without making approximations, let the state estimate vector for MBSU-SE

$$\hat{\mathbf{x}} = [\hat{V}_m \quad \hat{V}_m^1 \quad \dots \quad \hat{V}_m^{n_P}]^\top , \tag{2.127}$$

while the measurement vector

$$\mathbf{z} = [\mathbf{V}_M \quad \mathbf{I}_M]^\top . \tag{2.128}$$

The currents measured are related to the states via a conductance matrix found using appropriate KVL and KCL equations. The resulting $\mathbf{A}$ matrix is an $(n_P + 1) \times (n_P + 1)$ square matrix, while $\mathbf{b}$ is an $(n_P + 1) \times 1$ vector. Similarly, to solve the WLS problem for PDU-g without making approximations, let the state estimate vector

$$\hat{\mathbf{x}} = [\hat{V}_p^g \quad \hat{V}_1^g \quad \dots \quad \hat{V}_{n_L}^g]^\top , \tag{2.129}$$

while the measurement vector

$$\mathbf{z} = [\mathbf{V}_P^g \quad \mathbf{I}_P^g]^\top , \tag{2.130}$$

where $\mathbf{I}_P^g$ is the vector in (2.97). The resulting $\mathbf{A}$ matrix would be an $(n_L + 1) \times (n_L + 1)$ square matrix, while $\mathbf{b}$ would be an $(n_L+1)\times 1$ vector. With these $\hat{\mathbf{x}}$ and $\mathbf{z}$ vectors, we solve WLS problem (2.8)–(2.9) for the MBSU and PDUs. The σ_z and d_z of estimates obtained by using this WLS method is compared with the proposed method. The results are tabulated in Table 2.2.

From Table 2.2, we observe that d_z using both methods is small, indicating that, on an average, the estimates are very close to the actual value of the estimated quantity. The σ_z of estimates of variables using both methods are approximately equal. They are very close to the standard deviation (shown in the last column) calculated from the approximate analytical equations using the principle of propagation of uncertainty.

2.5.2 Comparison with centralized state estimation

In a centralized SE architecture, a central processor collects measurements by all the sensors in the system. It uses all these measurements to estimate the currents and voltages throughout the system. We now compare the accuracy of estimates obtained using the proposed method with that obtained from a centralized formulation. In case of the centralized SE problem, let the state estimate vector

$$\hat{\mathbf{x}} = [\hat{V}_m \quad \hat{V}_m^1 \quad \dots \quad \hat{V}_m^{n_P} \quad \hat{V}_p^1 \quad \hat{V}_1^1 \quad \dots \quad \hat{V}_{n_L}^1 \quad \hat{V}_p^2 \quad \hat{V}_1^2 \quad \dots \quad \hat{V}_{n_L}^2]^\top \tag{2.131}$$

The measurement vector contains all PDU and MBSU measurements. Thus,

$$\mathbf{z} = [\mathbf{V}_M \quad \mathbf{V}_P^1 \quad \dots \quad \mathbf{V}_P^{n_P} \quad \mathbf{I}_M \quad \mathbf{I}_P^1 \quad \dots \quad \mathbf{I}_P^{n_P} \quad \mathbf{0}_{1\times n_P}]^\top \tag{2.132}$$

where $\mathbf{I}_P^g$ is the vector from (2.97), and $\mathbf{0}_{1\times n_P}$ is a vector of zeroes. The zero measurements are used to represent the following KCL equation in terms of the states:

$$\frac{\hat{V}_m^g - \hat{V}_p^g}{R_p} + \sum_{h=1}^{n_L} \frac{V_h^g - V_p^g}{R_s} = 0\,, \qquad \forall g \in \{1, \dots, n_P\}\,. \tag{2.133}$$

The weights associated with zero measurements are taken as $100\sigma_i$ to ensure that (2.133) is satisfied in the WLS solution. All the other measurements can be expressed in terms of the voltages in the state vector via KVL and KCL relations. Table 2.3 shows the comparison of

Table 2.3. Accuracy comparison

Variables	Centralized architecture		Proposed architecture	
	$d_z(\%)$	σ_z	$d_z(\%)$	σ_z
PDU voltages	1.8×10^{-4}	21.6 mV	$2.0\ \times10^{-4}$	30.6 mV
PDU currents	5.0×10^{-2}	176.1 mA	17.1×10^{-2}	163.6 mA
MBSU voltages	1.2×10^{-4}	21.2 mV	6.2×10^{-4}	37.9 mV
MBSU to PDU currents	1.3×10^{-3}	68.7 mA	3.1×10^{-2}	144.3 mA
Converter to MBSU current	1.3×10^{-3}	137.3 mA	1.5×10^{-3}	124.6 mA

accuracy between the centralized and proposed formulation in terms of d_z and σ_z. Overall, we obtain slightly more accurate estimates using a centralized formulation.

2.5.3 Identification of biased sensors

In this section, the ability of the modified LNR test to detect faults is statistically tested. In particular, we test the ability to identify bias in the PDU current sensors, given the additional sensors found in section 2.4.2. If we suspect bad data being measured by the same sensor 4 or more times out of 5 consecutive sets of measurements, we declare that sensor as faulty.

For PDU currents, a bias b increasing in magnitude from 0 to 3 A in steps of 0.05 A was introduced in each of the $n_L + 3 = 11$ sensors, one at a time. In Fig. 2.6, the plots show the percentage of cases declaring fault in sensor-$l, \forall l \in \{1, \ldots, n_L + 3\}$, when the faulted sensor is the one measuring I_1^1 (sensor 1), I_5^1 (sensor 5), I_7^1 (sensor 7), I_{A1}^1 (sensor 9), I_{A2}^2 (sensor 10), and I_m^1 (sensor 11), respectively.

Thus, using the LNR test, we can identify biased PDU current sensors when the additional sensors are included.

2.5.4 Reestimation after sensor fault detection

After sensor fault is detected in a current or voltage sensor, we remove the corresponding incorrect measurement, and reestimate the system state.

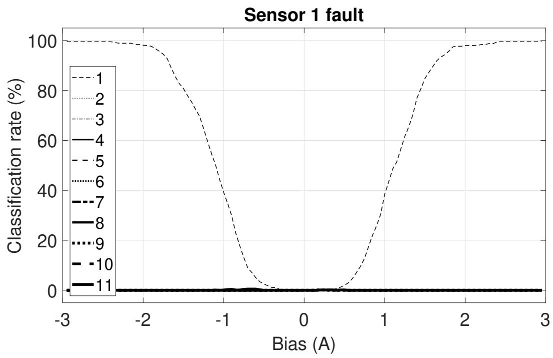

(a) Bias in sensor measuring I_1^1.

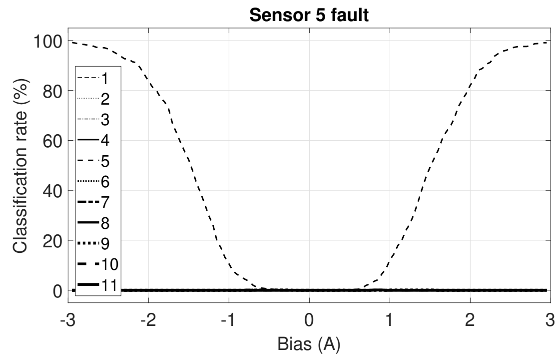

(b) Bias in sensor measuring I_5^1.

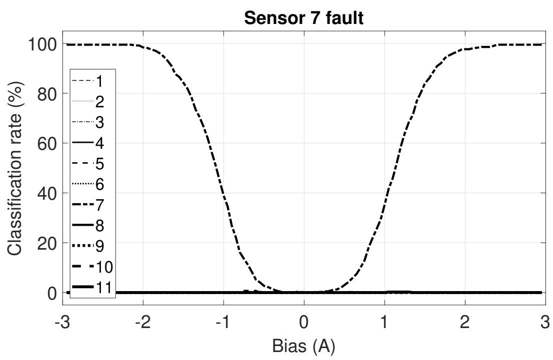

(c) Bias in sensor measuring I_7^1.

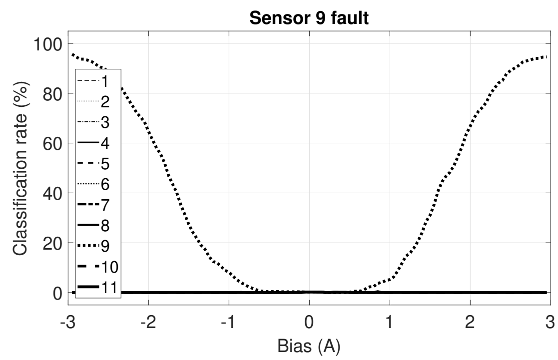

(d) Bias in sensor measuring I_{A1}^1.

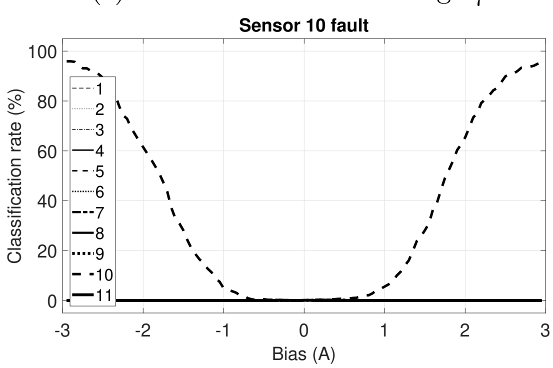

(e) Bias in sensor measuring I_{A2}^1.

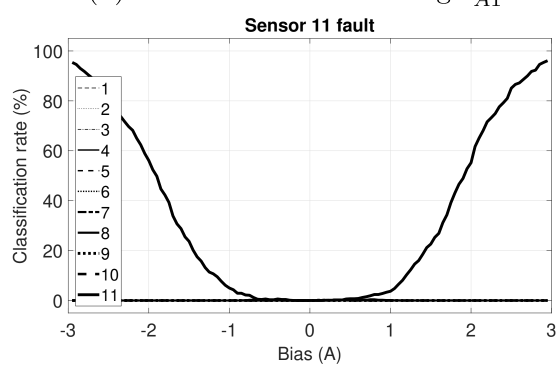

(f) Bias in sensor measuring I_m^1.

Figure 2.6. Plots showing classification rate when PDU current sensors are biased.

Consider a fault in voltage sensor of load 1 of PDU-1 (measuring V_1^1). We inject a bias of 0.75 V in the sensor in all $R = 2000$ studies. If the biased measurement is not removed, the d_z of the voltage estimates becomes 6.2×10^{-2} compared to 2.0×10^{-4}, when all measurements are healthy (Table 2.2). However, using the LNR test, we correctly identify the biased sensor. Thus, if the biased measurement is removed, and we perform SE using the remaining measurements, $d_z = 5.9 \times 10^{-4}$, thus indicating much more accurate estimates.

3. FAULT DIAGNOSIS IN POWER ELECTRONIC CONVERTERS

The capability to detect and identify faults within power electronic converters is crucial for critical applications such as spacecraft power systems. This chapter presents a machine learning approach to accurately and reliably diagnose faults in a dc-dc converter system. The proposed algorithm employs support vector machines (SVM), a supervised machine learning technique, to classify various conditions of a converter. To determine the condition of the converter, the proposed method utilizes features related to the power spectrum of the converter input current.

3.1 Support Vector Machine (SVM) preliminaries

Support Vector Machine (SVM) is a supervised machine-learning method, popular for classification of unknown data into predetermined categories known as classes. Data points of a class are characterized by certain known features, which differentiate them from samples of other class(es). Data samples whose classes are known are labeled according to their class, and fed as inputs to the SVM algorithm. Such data points are known as training samples because they are used to train the SVM model. Training the SVM model implies finding the function(s) that best separates the data points of different classes. The SVM algorithm, thus, comprises of an optimization problem that needs to be solved as part of the training process. Once trained, the SVM model can determine the class of samples that are not already labeled.

Consider the problem of classifying samples of 2 classes, that are labeled as '+1' and '-1' [46]. A training sample $\mathbf{x}_u$ is an $n_f \times 1$ vector, whose elements are its features, with y_u as its class label. Thus, $\mathcal{S} = \{(\mathbf{x}_u, y_u) \,|\, \mathbf{x}_u \in \mathbb{R}^{n_f},\, y_u \in \{1, -1\},\, u \in \{1, \ldots, s\}\}$ is the training dataset having s training samples. A hyperplane described by the equation

$$\mathbf{w}^o \mathbf{x} + w_0^o = 0 \tag{3.1}$$

separates samples of the two classes, where $\mathbf{w}^o$ is a $1 \times n_f$ vector of coefficients.

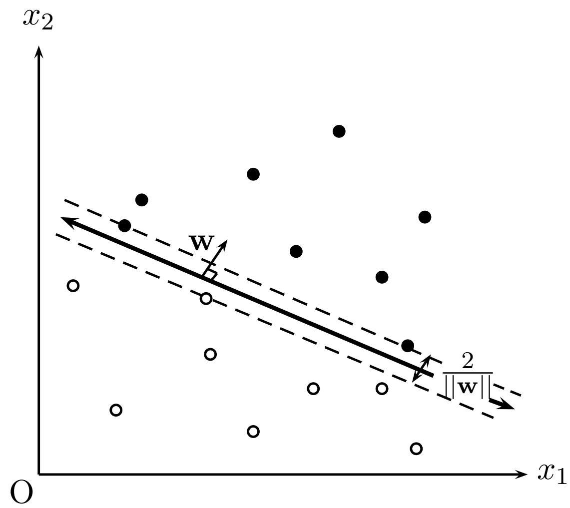

Figure 3.1. Maximal margin classification of 2 class samples.

For instance, consider a classification problem in $\mathbb{R}^2$, as shown in Fig. 3.1. The shaded and unshaded circles represent individual training samples of classes labeled '+1' and '-1' respectively. The two dashed lines, parallel to the classifier $\mathbf{w}^o\mathbf{x} + w_0^o = 0$, and passing through some of the training samples are called support lines. They are equidistant from the classifier. Hence, let these support lines be represented by the equations $\mathbf{w}^o\mathbf{x} + w_0^o = w_c$ and $\mathbf{w}^o\mathbf{x} + w_0^o = -w_c$, respectively. By substituting $\mathbf{w} = \mathbf{w}^o/w_c$, they can be also be represented by $\mathbf{w}\mathbf{x} + w_0 = 1$ and $\mathbf{w}\mathbf{x} + w_0 = -1$, respectively. The perpendicular distance between the support lines, called the margin, is equal to $2/||\mathbf{w}||$. So, to maximize this margin, the problem is formulated as

$$\max_{\mathbf{w},w_0} \frac{2}{||\mathbf{w}||} \tag{3.2}$$

subject to:

$$\mathbf{w}\mathbf{x}_u + w_0 \geq 1\,, \qquad u : y_u = 1\,, \tag{3.3a}$$

$$\mathbf{w}\mathbf{x}_u + w_0 \leq -1\,, \quad u : y_u = -1\,, \tag{3.3b}$$

To relax the requirement that all training samples of a class need to be separated from all samples of the other class by the optimal classifier, slack variables ξ_u, $\forall u \in \{1, \ldots, s\}$, are introduced. The inequality constraints (3.3) are modified to

$$y_u(\mathbf{w}\mathbf{x}_u + w_0) \geq 1 - \xi_u\,, \quad \forall u \in \{1, \ldots, s\}\,. \tag{3.4}$$

To limit the number of misclassified samples and the magnitude of the slack variables, a penalty term, $\kappa \sum_{u=1}^{N_s} \xi_u$ is introduced in the objective, where $\kappa > 0$ is the cost of misclassification. Thus, the problem is modified to the following:

$$\min_{\mathbf{w}, w_0, \xi} \frac{1}{2} \, ||\mathbf{w}||^2 + \kappa \sum_{u=1}^{N_s} \xi_u \tag{3.5}$$

subject to:

$$y_u(\mathbf{w}\mathbf{x}_u + w_0) \geq 1 - \xi_u\,, \qquad u \in \{1, \ldots, s\}\,, \tag{3.6a}$$

$$\xi_u \geq 0\,, \qquad u \in \{1, \ldots, s\}\,. \tag{3.6b}$$

After some manipulation, the dual problem can be written as:

$$\min_{\Lambda} \frac{1}{2} \sum_{u=1}^{s} \sum_{v=1}^{s} \lambda_u \lambda_v y_u y_v \mathbf{x}_u^\top \mathbf{x}_v - \sum_{v=1}^{s} \lambda_v \tag{3.7}$$

subject to

$$\sum_{v=1}^{s} \lambda_v y_v = 0\,, \tag{3.8a}$$

$$\lambda_v \geq 0\,, \qquad v \in \{1, \ldots, s\}\,, \tag{3.8b}$$

$$\lambda_v \leq \kappa\,, \qquad v \in \{1, \ldots, s\}\,. \tag{3.8c}$$

where $\Lambda = \{\lambda_1, \ldots, \lambda_s\}$ is a vector of Lagrangian multipliers. Solving this convex quadratic optimization problem yields the solution $\Lambda^* = \{\lambda_1^*, \ldots, \lambda_s^*\}$. Then, the optimal hyperplane can be found as

$$\mathbf{w}^*\mathbf{x} + w_0^* = 0\,, \tag{3.9}$$

where, using any sample, (say, sample number $v \in \{1, \ldots, s\}$),

$$w_0^* = y_v - \sum_{u=1}^{s} \lambda_u^* y_u (\mathbf{x}_u^\top \mathbf{x}_v) \,, \tag{3.10}$$

$$\mathbf{w}^* = \sum_{u=1}^{s} \lambda_u^* y_u \mathbf{x}_u^\top \,. \tag{3.11}$$

Putting (3.10) and (3.11) in (3.9), we can determining the optimal hyperplane. Based on that, a decision function $t(\mathbf{x})$ can be defined as

$$t(\mathbf{x}) = \sum_{u=1}^{s} \lambda_u^* y_u (\mathbf{x}_u^\top \mathbf{x}) + w_0^* \tag{3.12}$$

The $\mathrm{sgn}(t(\mathbf{x}_T))$ is the class of a test sample $\mathbf{x}_T$.

If samples of the two classes are linearly inseparable in the n_f-dimensional space, they can be mapped to an m_f-dimensional space where they are linearly separable through a mapping function $p(\mathbf{x})$. Then, the optimal hypersurface $\mathbf{w}p(\mathbf{x}) + w_0 = 0$ is found by solving the optimization problem (3.5) with constraint (3.6a) modified to

$$y_u(\mathbf{w}p(\mathbf{x}_u) + w_0) \geq 1 - \xi_u \,, \quad u \in \{1, \ldots, s\} \,. \tag{3.13}$$

The objective (3.7) of the dual problem changes to

$$\min_{\Lambda} \frac{1}{2} \sum_{u=1}^{s} \sum_{v=1}^{s} \lambda_u \lambda_v y_u y_v p(\mathbf{x}_u)^\top p(\mathbf{x}_v) - \sum_{v=1}^{s} \lambda_v \tag{3.14}$$

The term $p(\mathbf{x}_u)^\top p(\mathbf{x}_v)$ can be replaced by a function $K(\mathbf{x}_u, \mathbf{x}_v) = p(\mathbf{x}_u)^\top p(\mathbf{x}_v)$, known as a kernel. In this work, we use the Radial Basis Function (RBF) kernel given by

$$K(\mathbf{x}_u, \mathbf{x}_v) = \mathrm{e}^{-\beta ||\mathbf{x}_u - \mathbf{x}_v||^2} \,, \tag{3.15}$$

where β is a constant that, along with penalty factor κ, can be tuned to better discriminate between samples. An unknown sample $\mathbf{x}_T$ is classified based on the side of the optimal hyperplane on which it lies, found by the sign of the decision function evaluated at $\mathbf{x}_T$ as

$$t_K(\mathbf{x}_T) = \sum_{u=1}^{s} \lambda_u^* y_u K(\mathbf{x}_u, \mathbf{x}_T) + w_0^* \tag{3.16}$$

where for any sample number $v \in \{1, \ldots, s\}$

$$w_0^* = y_v - \sum_{u=1}^{s} \lambda_u^* y_u K(\mathbf{x}_u, \mathbf{x}_T)\,. \tag{3.17}$$

In our problem, we simulate the converter under different conditions (classes) to obtain waveforms capturing the resultant input current signal. We generate a training sample from each waveform by computing certain features related to the power spectrum characterizing the signal. SVM classifiers are trained to recognize N_C classes, each corresponding to a different condition. Once trained, they can identify the condition of the converter using the measured input current signal.

3.1.1 Probabilistic output

As explained in the previous section, an input sample $\mathbf{x}_T$ is classified based on the sign of the function $t_K(\mathbf{x}_T)$. Our confidence in the resulting classification, i.e., the probability that it is correct, would depend on the proximity of the sample to the classifier as quantified by the magnitude of the decision value $t_K(\mathbf{x}_T)$. Intuitively, the larger the magnitude of $t_K(\mathbf{x}_T)$, the greater would be the probability of correct classification. Accordingly, a monotonic function from $(-\infty, \infty)$ whose range is $[0, 1]$ must be defined to map the decision value $t_K(\mathbf{x}_T)$ to the corresponding probability. A sigmoid is a common function [46], [47] relating these two quantities by

$$P(t_K) = \frac{1}{1 + \exp(a_1 t_K + a_2)}\,, \qquad a_1 < 0 \tag{3.18}$$

The value $P(t_K(\mathbf{x}_T))$ is the posterior class probability that the sample $\mathbf{x}_T$ belongs to the class y_T. The parameters of the sigmoid function, a_1 and a_2 are found by solving an optimization problem that maximizes the probability that the samples are being classified correctly.

Along with the determined class of a sample, we utilize the posterior probability of it belonging to the class in order to identify the condition of the converter.

3.2 Feature Selection

As explained in the previous section, each sample is characterized by certain features that help in determining its class. Thus, we must select a set of n_f features that allow us identify the condition of the converter.

When a fault or step change occurs in a converter system, transients are generated in the input current, and its subsequent waveform may change. Depending on the type of fault, the signal characteristics may differ. Thus, we select features related to the frequency components present in the subsequent waveform. Consider a signal x sampled at a frequency f_s. A window of L consecutive samples of the signal $[x^{(1)}, \ldots, x^{(L)}]$ is taken. Each window corresponds to a data sample. A Discrete Fourier Transform (DFT) of the signal is performed, and sample features based on the average power in predominant frequency bands are computed. The k-th frequency component of the signal

$$X_k = \sum_{m=1}^{L} x^{(m)} \mathrm{e}^{-j\frac{2\pi k m}{L}} . \tag{3.19}$$

The J-th feature $\mathbf{x}^J$ of sample $\mathbf{x}$ corresponding to this window is computed as

$$\mathbf{x}^J = \log\left(\sum_{k=k_J-D}^{k_J+D} |X_k|^2\right) , \tag{3.20}$$

where k_J is a component in the DFT selected to characterize the waveform, and D is the number of frequency components on either side of k_J selected to represent a frequency band.

Thus, DFT of each window of L consecutive samples will be performed and its features will be computed according to (3.20).

3.3 Training

This section explains how SVM-classifiers are trained to identify different conditions of the converter system. We wish to identify events of not two, but N_C types. Thus, a binary classifier discriminating between class-C and the remaining $N_C - 1$ classes is generated, $\forall\, C \in N_C$.

Training samples of each class are needed to generate a classifier (the optimal hyperplane). To obtain them, we sample several input current waveforms (having L consecutive measurements) of the converter at a sampling frequency f_s. Each window shows the transition from normal to the considered condition under different loading levels and other random variations. The n_f features characterizing each waveform are computed using (3.20) resulting in a corresponding sample $\mathbf{x} \in \mathbb{R}^{n_f}$.

When finding the C-th classifier, samples belonging to class-C are labeled as '+1' while all the remaining samples from the training data set are labeled '-1'. This produces N_C classifiers, each of which determines whether an unknown sample belongs to its own class or not.

To find the constants β and κ for each classifier, we use B-folded cross-validation. It is a process in which the training data is first split into B subsets containing equal samples. Then, for some value of the pair (β, κ), the classifiers are trained on one data subset and tested on the remaining $B-1$ subsets, and this process is repeated for each subset. Since the labels of training samples are known, the misclassified samples in the remaining $B-1$ subsets are counted. The objective is to select β and κ so that the average percentage of misclassified samples, over the B times that this process is repeated, is minimized. Thus, a grid-search is performed for finding the pair (β, κ) that minimizes this objective.

The optimal classifiers so determined are used to identify the class of an unlabelled sample.

3.4 Testing

The objective is to determine to which class an incoming measured signal belongs to indicate the system condition.

Fig. 3.2 shows the algorithm used to identify the system conditions. At any point in time, the past L signal measurements are captured. The signal features for this window of L consecutive samples in time $(x_T^{(a-L+1)}, \ldots, x_T^{(a)})$ are computed using (3.20). The sample $\mathbf{x}_T$ (corresponding to this window) so characterized is tested against each of the N_C binary classifiers. The sign of the decision function of each classifier C predicts whether $\mathbf{x}_T$ belongs

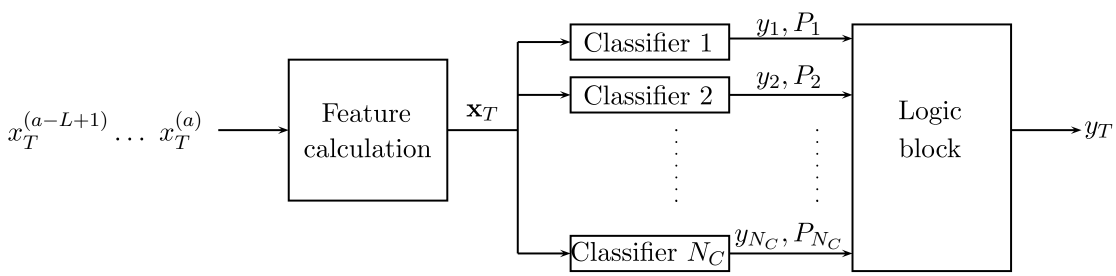

Figure 3.2. SVM-based algorithm for classifying events.

to its class or not by returning the label $y_C \in \{1, -1\}$, respectively. Using the trained sigmoid models (3.18), the posterior probability P_C of this classification is calculated. Thus, the output of this step is a prediction of whether $\mathbf{x}_T$ belongs to class-C, $C \in \{1, 2, \dots, N_C\}$ or not, along with a corresponding posterior probability P_C.

The logic block decides the class $y_T \in \{1, \dots, C\}$ of the sample as follows: If only one classifier predicts that the sample belongs to its class-C by returning $y_C = 1$ with a posterior probability $P_C \geq P_t$ (set threshold), the class of the event is identified as C. However, if $P_C < P_t$, $\forall\, C \in \{1, 2, \dots, N_C\}$ or if more than one classifier declares that the event belongs to a particular class with $P_C \geq P_t$, the sample remains unclassified. This condition helps us avoid false alarms.

3.5 Results

The algorithm is tested on the converter system shown in Fig. 3.3. The circuit consists of two back-to-back 3-phase interleaved dc-dc converters connected via a 30 V dc link. The input to the module is a 24 V dc voltage source, and a constant power load (CPL) is connected at the 24 V output. MOSFETs are employed as switches in the circuit. The circuit parameters are shown in Table 3.1. The switching frequency is 30 kHz. Voltages v_{dc} and v_o are regulated. Noise is added in the measured input current signal (i_i), and quantization by the current sensor is taken into account.

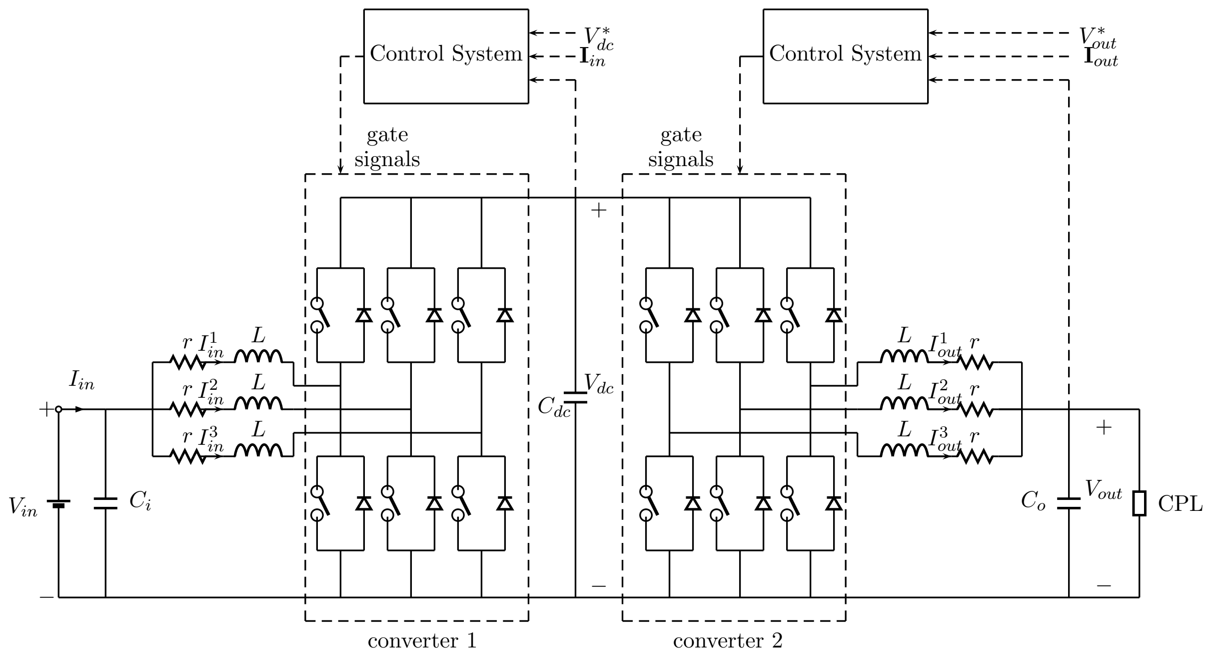

Figure 3.3. Back-to-back dc-dc converter circuit.

Table 3.1. Circuit parameters

Component	Value
Capacitor C_{i}	38.7 µF
Capacitor C_o	38.7 µF
Capacitor C_{dc}	67.2 µF
Inductor L	44.0 µH
Resistor r	16.0 mΩ
Constant power load	50 – 600 W
Fault resistance	0 – 0.1 Ω

The conditions identified are shown in Table 3.2. By running 5 ms-long simulations, 200 training samples of each of the $N_C = 8$ classes were obtained. For class 1–7 simulations, the corresponding fault or step change was inserted at $t = 1.5$ ms. The input current (i_i) waveform was sampled at $f_s = 360$ kHz. Thus, each training sample corresponds to a window of current signal with $L = 5 \text{ ms} \times f_s = 1800$ consecutive measurements in time. Frequencies 1 kHz, 2 kHz, . . . , 14 kHz, 30 kHz, and 60 kHz with $D = 2$, were used to compute the features. The feature corresponding to the dc component of the signal was also included in the set, leading to a total of 17 features. To obtain the parameters (β, κ) for each classifier, 3-folded cross-validation was used.

Table 3.2. Event classes

Class	Event
1	Load shorted
2	DC-link capacitor shorted
3	Lower switch of a phase leg of converter 1 open circuited
4	Upper switch shorted and lower switch open circuited in a phase leg of converter 1
5	Upper switch open circuited in a phase leg of converter 2
6	Upper switch open circuited and lower switch shorted in a phase leg of converter 2
7	Step change in load
8	Normal operation with no change

Testing samples were generated by running 100 more 15 ms-long simulations of each class. The input current signal under each condition is shown in Fig. 3.4. In these simulations, the system operated normally until $t = 6.5$ ms when the fault or step-change was inserted, except in case of class-8. The threshold posterior probability P_t was set to 0.9.

The percentage of samples of class-C that were classified as class-F, $\forall\, F \in \{1, \ldots, 8\}$ with respect to time was visualized using plots, here defined as confusion plots. Confusion plots of samples of different classes are shown in Fig. 3.5 and 3.6. None of the samples of class-C in these plots were classified as other than class-C or class-8, over time. Hence, for simplicity, their percentages were not plotted.

For the first few milliseconds, 100% of the samples were classified as the "normal no-change" condition (class-8) because there was no disturbance in the system. The windows that followed were either correctly classified as class-C or stayed unclassified. After $t = 6.5$ ms, the tested windows captured a portion of the transient. Hence, the percentage of correctly classified samples (referred to as the classification accuracy) shot up. The classification accuracy was invariably 100% at $t = 10$ ms because the tested window (capturing waveform data from $t = 5$–10 ms) matched with the training window, in that the condition is introduced at $t = 1.5$ ms after the beginning of the window. After 11.5 ms, the classification accuracy

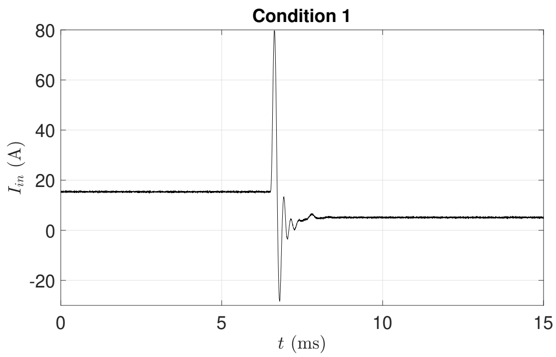

(a) Condition 1

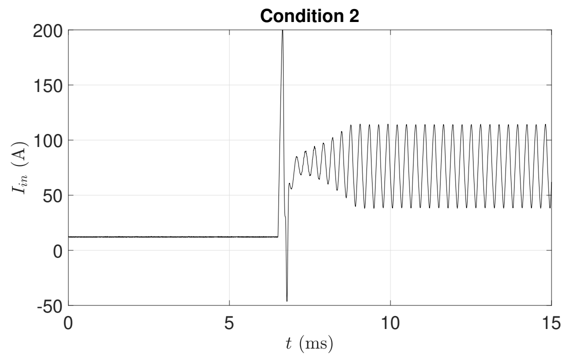

(b) Condition 2

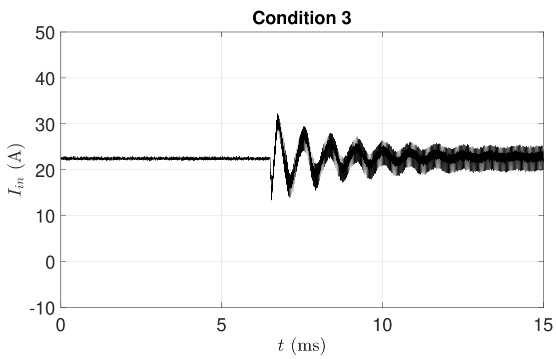

(c) Condition 3

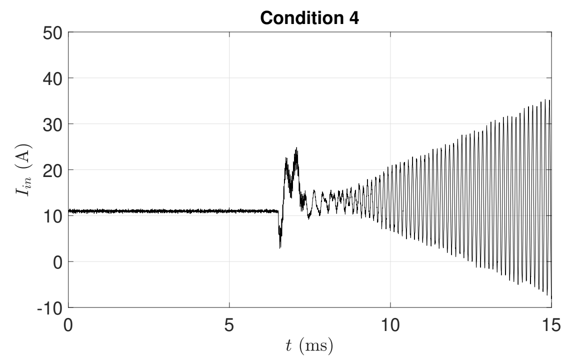

(d) Condition 4

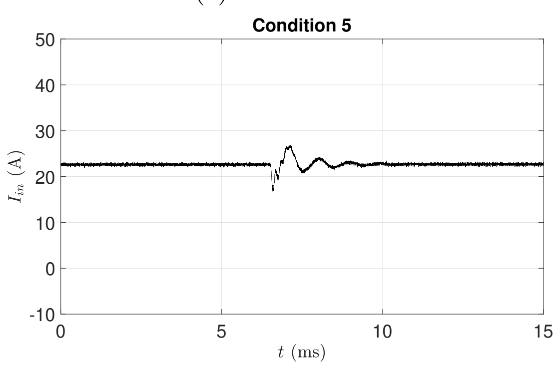

(e) Condition 5

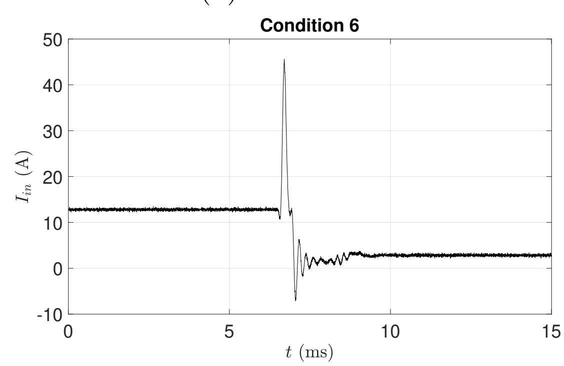

(f) Condition 6

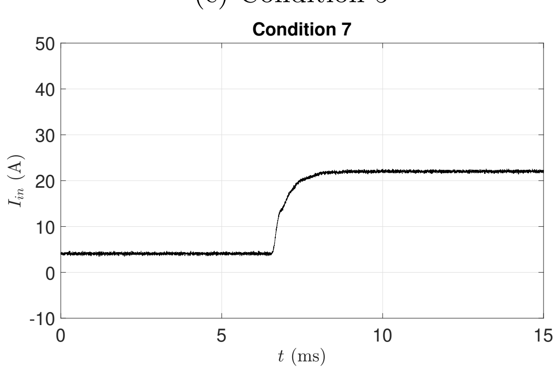

(g) Condition 7

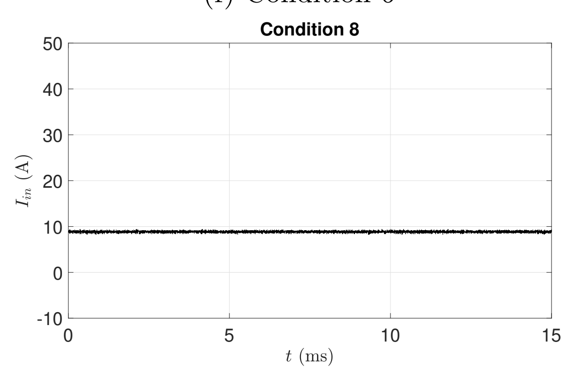

(h) Condition 8

Figure 3.4. Input current signal under each condition.

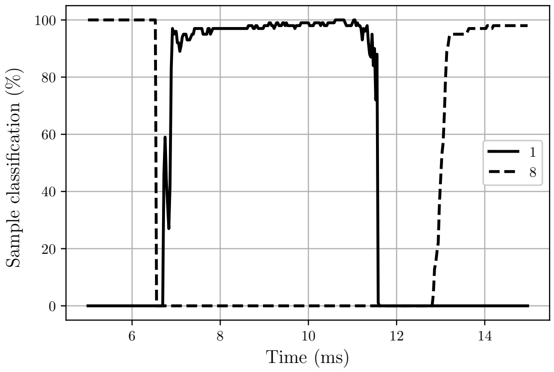

(a) Class 1 confusion plot.

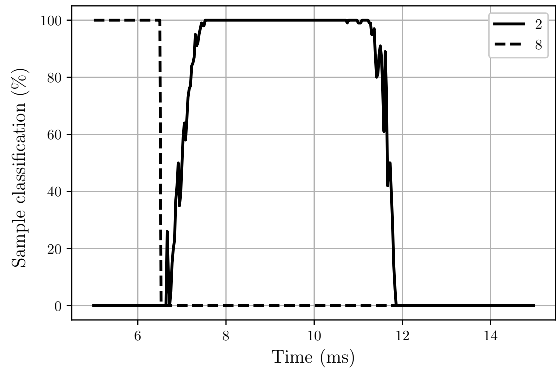

(b) Class 2 confusion plot.

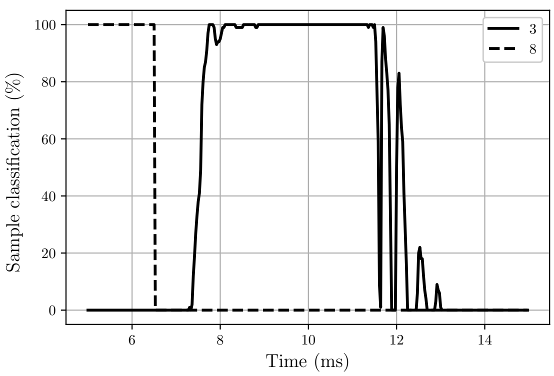

(c) Class 3 confusion plot.

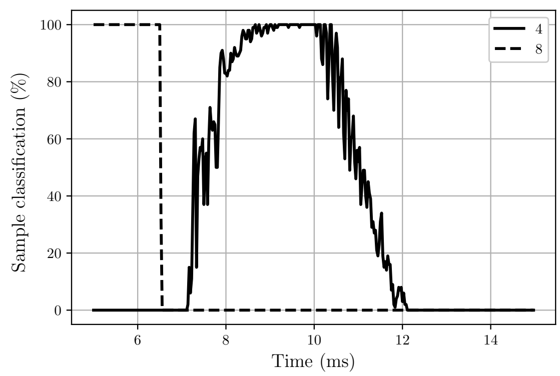

(d) Class 4 confusion plot.

Figure 3.5. Confusion plots when events 1–4 occur.

dropped because the window no longer captured any portion of the waveform behaviour with which the classifier was trained.

Thus, the algorithm is able to accurately and reliably identify the type of system condition that it has been trained to recognize.

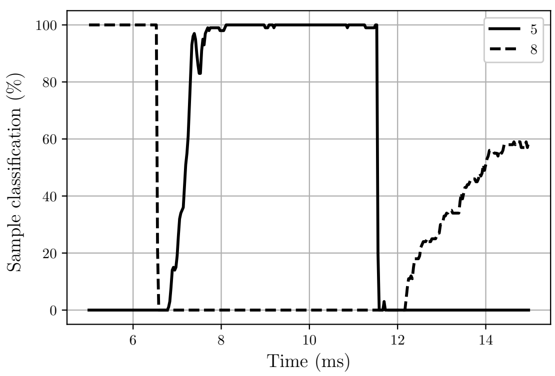

(a) Class 5 confusion plot.

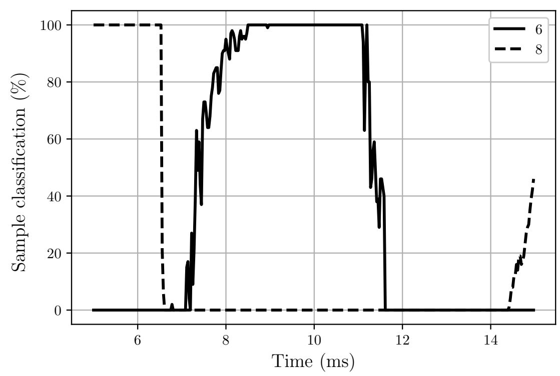

(b) Class 6 confusion plot.

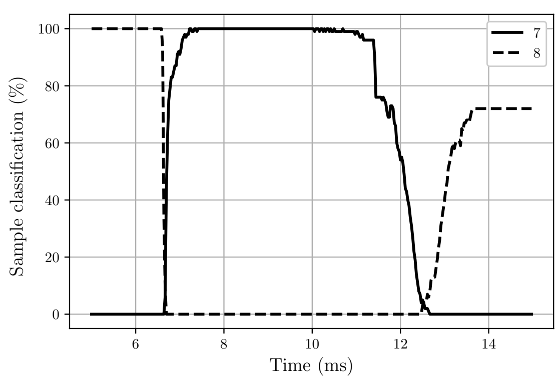

(c) Class 7 confusion plot.

Figure 3.6. Confusion plots when events 5–7 occur.

4. OPTIMAL POWER DISPATCH

In this chapter, we define the operational logic of an autonomous control system that ensures optimal system operation under normal and faulted conditions. A computer-based mission manager (MM) determines the desired load schedule that includes individual load demands and their respective priorities for a time horizon encompassing a few hours [2]. The autonomous control system then decides an optimal load dispatch that meets all operational constraints, while ensuring service to important loads. If a fault occurs in the power system, it is operated in a restorative state. This may involve rerouting power supply to loads by utilizing alternate paths and/or charging batteries at a lower rate. The proposed algorithm combines network reconfiguration with an optimal power flow. The associated mathematical formulation is relatively simple and computationally efficient.

Our system has three types of binary variables, namely, loads that can be switched on and off, decisions that choose appropriate battery charging rates, and switch states that determine the network topology. For a deep space vehicle, the speed of obtaining a solution is more important than its accuracy, especially when restoring the system after a fault. Therefore, the proposed approach is to use only the load on/off commands and battery-charging rate decisions as binary variables in the OPF problem. This leads to a mixed-integer linear program (MILP) that is efficiently solved using a software package called Gurobi. The OPF is a sub-problem embedded inside an outer loop over all network configurations.

4.1 System description

Fig. 4.1 shows the power system of a notional deep space vehicle based on the architecture set forth in [48]. The batteries and solar arrays are interfaced with power electronic converters (BCDUs and SARs, respectively). The power distribution units (PDUs) provide power to several loads. There are two main bus switching units (MBSUs) that can be tied together by closing switches S_X^1 and S_X^2, which are normally open. Under normal conditions, when the system is electrically divided in two parts, the voltage of each MBSU node is regulated to a nominal value, $V_{\text{nom}} = 120$ V. We define the following sets: all nodes $\mathcal{N} = \{1, \ldots, n_N\}$, MBSU nodes $\mathcal{M} = \{m_1, m_2\} \subset \mathcal{N}$, SAR output nodes $\mathcal{A} \subset \mathcal{N}$, PDU nodes $\mathcal{D} \subset \mathcal{N}$, and

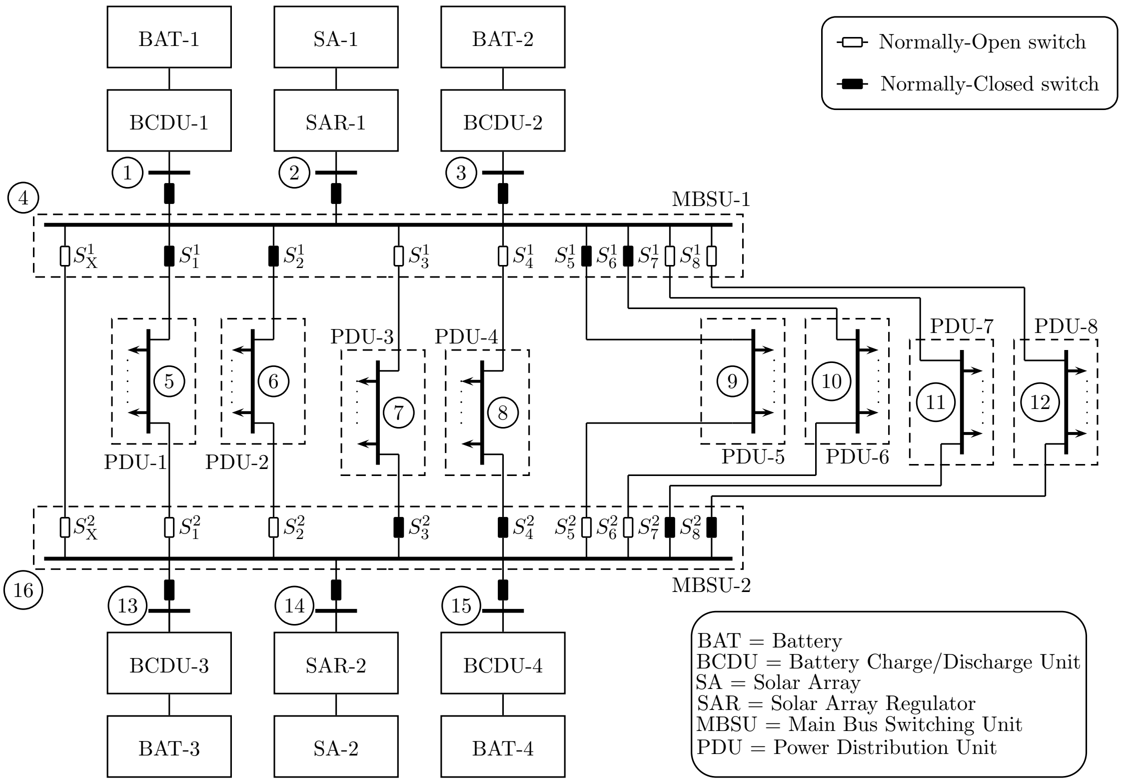

Figure 4.1. Notional deep space power system.

BCDU terminal nodes $\mathcal{B} \subset \mathcal{N}$. The conductance of line $l_{s,r}$ between nodes s and $r \in \mathcal{N}$ is denoted by $G_{s,r}$. There are $n_N = 16$ nodes, $n_P = 8$ PDUs, and $n_B = 4$ batteries. The PDUs are normally connected to one of the MBSUs based on their location via the shorter cable (for lower resistance). Thus, for PDU-1 through PDU-4, it is assumed that $G_{5,4} = G_{6,4} = G_{7,16} = G_{8,16} < G_{5,16} = G_{6,16} = G_{7,4} = G_{8,4}$. A similar assumption is made for the cables connecting PDU-5 through PDU-8.

4.1.1 Solar arrays

Arrays SA-1 and SA-2 receive solar energy in a 60 minute-long period of insolation, during which they can generate up to $P_{s,\max,k} = 30$ kW (assumed constant for simplicity), where the index $k \in \{k_1, \ldots, k_T\}$ denotes the time interval. In a subsequent 30 minute-long period of eclipse, $P_{s,\max,k} = 0$ kW [2]. The assumed SAR efficiency is $\eta_s = 0.95$.

4.1.2 Loads

Each PDU handles roughly 3 kW at peak load. The desired load schedule is decided by the MM [2]. The power demanded by load h on PDU-g at time k is denoted as $P^{g}_{Dh,k}$. All loads are assumed to be constant power loads, in the sense that they draw the needed power regardless of the voltage at the PDU bus. If load h connected to PDU-g is "binary", then $b^{g}_{h} \in \{0, 1\}$ is a decision variable for turning it off or on, respectively. Otherwise, if the load power can be adjusted in a continuous manner, the corresponding decision variable is $c^{g}_{h} \in \mathbb{R}$, $0 \leq c^{g}_{h} \leq 1$. We assume that $n_b = 4$ binary loads and $n_c = 4$ continuous loads are connected to each PDU, and denote the total number of loads at each PDU as $n_L = n_b + n_c$. Each load is assigned a corresponding weight $W^{g}_{h,k} \geq 0$ for every time interval k, such that higher weight implies greater importance. Loads have been classified as non-vital ($W^{g}_{h} = 1$), semi-vital ($W^{g}_{h} = 50$), and vital ($W^{g}_{h} = 500$).

4.1.3 Batteries

The batteries are based on a 2.6-Ah lithium ion cell [49]. The variation of the cell open-circuit voltage e with its state-of-charge (SoC), denoted by z, is shown in Fig. 4.2 [50]. A piecewise cubic Hermite interpolant is derived from the data points. The battery packs have $n_p = 14$ parallel strings of $n_s = 36$ cells in series. Assuming that the SoC of individual cells is the same, the batteries are modeled by a simple equivalent circuit [51] such that the battery terminal voltage v_B and current i_B are related by

$$v_B(z, i_B) = n_s e(z) - i_B R_B \,, \tag{4.1}$$

where the internal cell resistance $r_c = 20$ mΩ. Hence, the battery equivalent resistance is $R_B = n_s r_c / n_p = 51$ mΩ. The coulombic efficiency η_c relates to the amount of charge transferred to or from the battery cells (a fraction of charge is lost in electrochemical side reactions). Thus, the variation of the battery SoC with time is found using

$$\frac{dz}{dt} = -\frac{\eta_c i_B}{Q} \,, \tag{4.2}$$

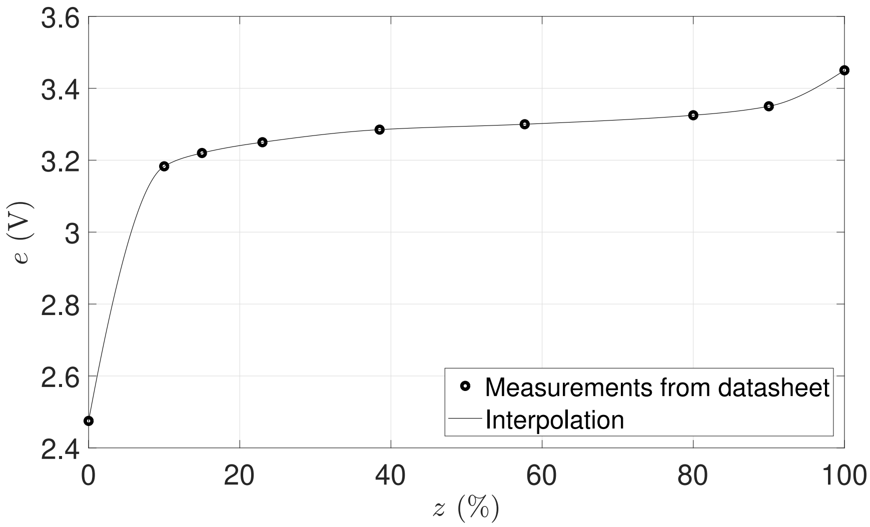

Figure 4.2. Cell open-circuit voltage vs. state of charge.

where Q is the battery capacity in coulombs. We assume charging $\eta_c = 0.99$, discharging $\eta_c = 1$, and BCDU energy conversion efficiency $\eta_B = 0.9$.

At the beginning of each insolation or eclipse period, or following a system fault, the SoC of each battery in the system is obtained from the battery management system. This initial SoC (z_0) and $i_B(t)$ serve as model inputs, and are used to determine the battery charging or discharging profiles. To maintain the long-term health of the batteries, the SoC is not allowed to drop below $z_{\min} = 20\%$ or to exceed $z_{\max} = 90\%$.

Charging

Charging is initially performed with current at a constant rate until a desired terminal voltage is reached, after which constant-voltage mode is employed [52]. The constant initial charging current i_B can be represented with an equivalent C-rate, which is the charging/discharging current relative to its nominal capacity Q. Thus, a yC rate refers to the current that would fully charge/discharge the battery in $1/y$ hours (assuming $\eta_c = 1$). Since batteries are the only source of energy during an eclipse, charging them to the fullest level possible is of paramount importance. Hence, charging is not delayed and starts at the very beginning of insolation.

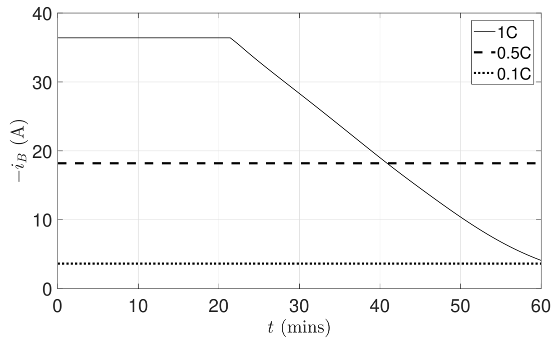

(a) Battery input current.

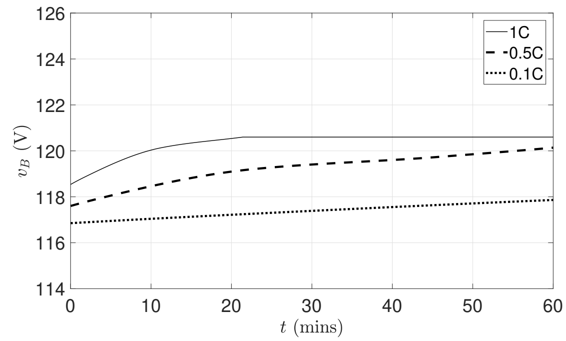

(b) Battery terminal voltage.

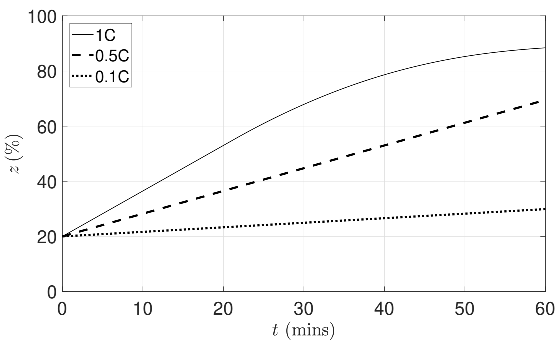

(c) Battery state-of-charge.

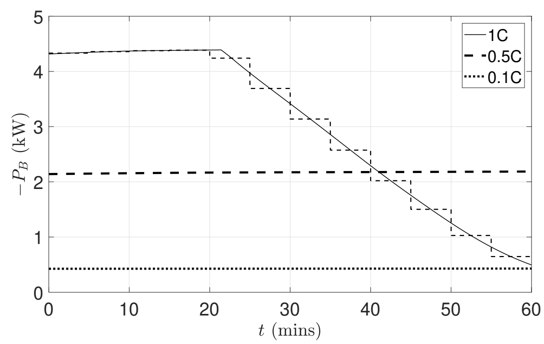

(d) Battery input power.

Figure 4.3. Battery charging profiles using constant-current constant-voltage method.

We define a set of n_R predetermined charging C-rates, $\mathcal{Y} = \{y_1, \ldots, y_{n_R}\}$. Examples of battery charging profiles for $z_0 = 0.2$ with $\mathcal{Y} = \{0.1, 0.5, 1\}$ are shown in Fig. 4.3. Constant-voltage mode is employed when $v_B = n_s e(z_{\max})$. The calculated power profile, $P_B(t) = v_B(t) i_B(t)$, is discretized by averaging over time intervals, as shown for the 1C rate case in Fig. 4.3. Similarly, for each BAT-g and with each charging rate $y_h \in \mathcal{Y}$, we compute the discretized input power $P^g_{Bh,k}$ at every interval k. Of these, only one power profile is selected for each battery.

Thus, we introduce binary decision variables $d^g_h \in \{0, 1\}$, $\forall g \in \{1, \ldots, n_B\}$ and $\forall h \in \{1, \ldots, n_R\}$, such that $d^g_h = 1$ implies that BAT-g is initially charged at C-rate y_h (and possibly later with constant voltage). In this study, we set $\mathcal{Y} = \{0, 0.1, 0.2, \ldots, 1\}$. Hence, there are $n_R = 11$ possible initial C-rates, including the trivial case of not charging.

The final SoC at the end of the charging period can be expressed as a function $z_f(z_0, y_h)$. The minimum C-rate needed to achieve $z_f \approx z_{\max}$ decreases with increasing z_0. Increasing

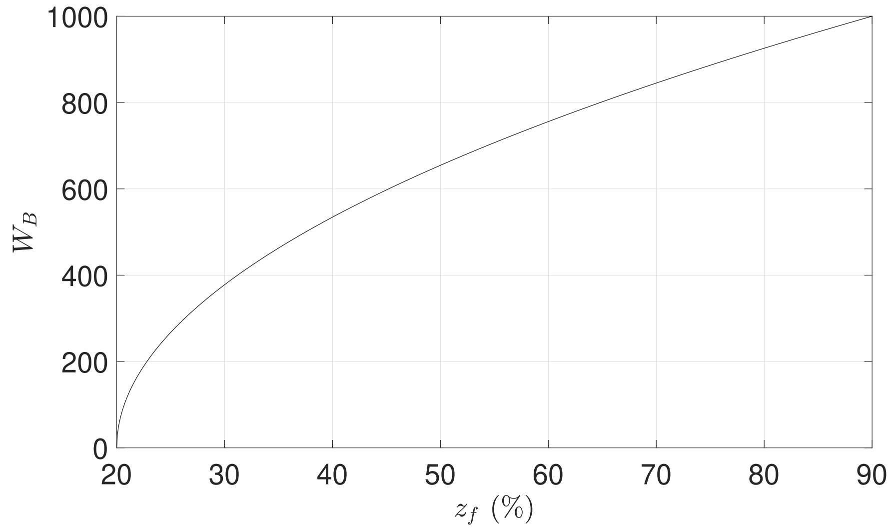

Figure 4.4. Weight for C-rate choices as a function of final SoC.

the C-rate above this value does not significantly increase z_f. Given that the objective of the charging strategy is to charge the batteries so that z_f reaches sufficiently close to $z_{\max}$, weights W_{Bh}^g corresponding to d_h^g are assigned based on

$$W_B(z_f) = W_{B\max}\sqrt{\frac{z_f - z_{\min}}{z_{\max} - z_{\min}}}, \tag{4.3}$$

where $W_{B\max} = 1000$. A plot of this function is shown in Fig. 4.4. The weights corresponding to C-rates achieving $z_f = 85$–90% have relatively small difference, which could lead to optimal solutions exhibiting a tradeoff between maximizing SoC and serving additional loads.

To summarize, for each BAT-g, the battery dynamic model takes z_0 as an input, computes a P_{Bh}^g profile and values of $z_f(z_0, y_h)$ for each considered C-rate, whence $W_B(z_f)$ is obtained. These parameters are provided to the optimization problem set forth in the next section.

Discharging

Batteries discharge during the eclipse period to supply power to the loads in a manner determined by the OPF, subject only to power and energy limits. In particular, the energy limit is determined as the energy $E_{Bg}(z_0)$ that BAT-g can provide when discharged continuously at the maximum allowed rate (here, 2C), from the time it starts discharging (t_1) until $z_{\min}$ is reached (say, at $t_{\min}$),

$$E_{Bg}(z_0) = \int_{t_1}^{t_{\min}} P_B^g(t)\, \mathrm{d}t\,. \tag{4.4}$$

4.2 OPF Formulation

The OPF is solved separately over insolation and eclipse periods. Time is discretized using an index $k \in \{k_1, \ldots, k_T\}$, forming intervals of duration Δt. The first interval k_1 may correspond to the beginning of insolation or eclipse, or it could be the first interval immediately after a fault (which may occur at any time instant). The final time interval k_T is always the final interval of the current period (insolation or eclipse). Power system injections from BCDUs, SARs, and PDUs are assumed positive. We define the following time-k vectors, assuming that at all PDUs, the continuous loads are listed after binary loads.

Binary and continuous load decision variables:

$$\mathbf{b}_k = \left[b_{1,k}^1, \ldots, b_{n_b,k}^1, \ldots, b_{1,k}^{n_P}, \ldots, b_{n_b,k}^{n_P}\right] \tag{4.5}$$

$$\mathbf{c}_k = \left[c_{n_b+1,k}^1, \ldots, c_{n_L,k}^1, \ldots, c_{n_b+1,k}^{n_P}, \ldots, c_{n_L,k}^{n_P}\right] \tag{4.6}$$

Net power injected at node s:

$$\mathbf{P}_k = \left[P_{s,k}\right], \qquad \forall s \in \mathcal{A} \cup \mathcal{B} \tag{4.7}$$

Line power between nodes s and r:

$$\mathbf{P}_{l,k} = \left[P_{s,r,k}\right], \qquad \forall s \in \mathcal{N}, r \in \mathcal{N} \tag{4.8}$$

Voltage at each node:

$$\mathbf{V}_k = \left[V_{s,k}\right], \qquad \forall s \in \mathcal{N} \tag{4.9}$$

Charging profile binary decision variables:

$$\mathbf{d} = \left[d_1^1, \ldots, d_{n_R}^1, \ldots, d_1^{n_B}, \ldots, d_{n_R}^{n_B}\right] \tag{4.10}$$

These variables are collected in $\mathbf{x}_k = [\mathbf{b}_k, \mathbf{c}_k, \mathbf{P}_k, \mathbf{P}_{l,k}, \mathbf{V}_k]$ and $\mathbf{x} = [\mathbf{x}_{k_1}, \mathbf{x}_{k_2}, \ldots, \mathbf{x}_{k_T}, \mathbf{d}]$.

4.2.1 OPF formulation during insolation

During insolation under normal conditions, the OPF problem is formulated as follows:

$$\max_{\mathbf{x}} \sum_{k=k_1}^{k_T} \sum_{g=1}^{n_P} \left\{ \sum_{h=1}^{n_b} b_{h,k}^g W_{h,k}^g + \sum_{h=n_b+1}^{n_L} c_{h,k}^g W_{h,k}^g \right\} + \sum_{g=1}^{n_B} \sum_{h=1}^{n_R} d_h^g W_{Bh}^g \tag{4.11}$$

subject to:

Approximate line power flow from $s \in \mathcal{N}$ to $r \in \mathcal{N}$:

$$P_{s,r,k} = V_{\mathrm{nom}} G_{s,r} \Big(V_{s,k} - V_{r,k} \Big) \,. \tag{4.12}$$

Power balance equation at node s:

$$P_{s,k} = \sum_{r \in \mathcal{N}} P_{s,r,k} \,, \qquad \forall s \in \mathcal{N} \,. \tag{4.13}$$

Power injection at node $s \in \mathcal{D}$ for the corresponding PDU-g:

$$P_{s,k} = -\sum_{h=1}^{n_b} b_{h,k}^g P_{Dh,k}^g - \sum_{h=n_b+1}^{n_L} c_{h,k}^g P_{Dh,k}^g \,. \tag{4.14}$$

Selection of only one charging profile for each battery:

$$\sum_{h=1}^{n_R} d_h^g = 1 \,, \qquad \forall g \in \{1, \ldots, n_B\} \,. \tag{4.15}$$

Power injection into node $s \in \mathcal{B}$ for charging BAT-g:

$$P_{s,k} = -\frac{1}{\eta_B} \sum_{h=1}^{n_R} d_h^g P_{Bh,k}^g \,, \qquad \forall s \in \mathcal{B} \,. \tag{4.16}$$

Reference node voltage:

$$V_{m,k} = V_{\text{nom}}\,, \qquad\qquad \forall m \in \mathcal{M}\,. \tag{4.17}$$

Node voltage constraints ($\pm 5\%$ around V_{nom}):

$$V_{s,\min} \le V_{s,k} \le V_{s,\max}\,, \qquad\qquad \forall s \in \mathcal{N}\,. \tag{4.18}$$

Power injection limits:

$$0 \le P_{s,k} \le \eta_s P_{s,\max,k}\,, \qquad\qquad \forall s \in \mathcal{A}\,. \tag{4.19}$$

4.2.2 OPF formulation during eclipse

During an eclipse under normal conditions, the OPF problem is formulated as follows:

$$\max_{\mathbf{x}} \sum_{k=k_1}^{k_T} \sum_{g=1}^{n_P} \left\{ \sum_{h=1}^{n_b} b_{h,k}^{g} W_{h,k}^{g} + \sum_{h=n_b+1}^{n_L} c_{h,k}^{g} W_{h,k}^{g} \right\} \tag{4.20}$$

with $\mathbf{x}_k = [\mathbf{b}_k, \mathbf{c}_k, \mathbf{P}_k, \mathbf{P}_{l,k}, \mathbf{V}_k]$ and $\mathbf{x} = [\mathbf{x}_{k_1}, \mathbf{x}_{k_2}, \ldots, \mathbf{x}_{k_T}]$,

subject to:

Equations (4.12)–(4.14), (4.17)–(4.19),

Power injection at node $s \in \mathcal{B}$ supplied by BAT-g:

$$\frac{\Delta t}{\eta_B} \sum_{k=k_1}^{k_T} P_{s,k} \le E_{Bg}(z_0)\,, \qquad \forall s \in \mathcal{B}\,. \tag{4.21}$$

BAT-g power injection limits:

$$0 \le P_B^g \le P_{B,\max}\,. \tag{4.22}$$

where $P_{B,\max}$ is determined by the maximum discharge rate of the battery.

Modifications made to the nominal formulation for various scenarios involving system faults are listed in Table 4.1 and further explained in the next section.

Table 4.1. Reconfiguration/OPF formulation under different scenarios

Condition	Constraint changes	Allowable combinations ($\mathcal{R}_a$)
Normal	–	[110011000]
Fault in SA-v	Reduce $P_{s,\max,k}$; (4.17) removed for $m_v \in \mathcal{M}$	Those with $S_X^1 = 1$
Fault in BAT-g	Set $P_{B,k}^g = 0$	$\mathcal{R}$
Line-to-ground fault in $l_{s,r}$	–	Those with switch in $l_{s,r}$ open
MBSU-v fault	Set $G_{s,m_v} = 0, s \in \mathcal{A} \cup \mathcal{B}$; (4.17) removed for $m_v \in \mathcal{M}$	$S_g^v = 0, \forall g \in \{1, \ldots, n_P\}$
SC fault of PDU-g at node $a \in \mathcal{D}$	Set $G_{a,m_v} = 0, m_v \in \mathcal{M}$	Those with $S_g^1 = 0$
SC fault on load h of PDU-g	Set $P_{Dh}^g = 0$	$\mathcal{R}$

4.3 Combined system reconfiguration and OPF algorithm

Reconfiguration involves making decisions about operating the switches $S_g^v \in \{0, 1\}$, $\forall g \in \{1, \ldots, n_P\}$, and $S_X^v \in \{0, 1\}$, $v \in \{1, 2\}$. A PDU is connected to just one MBSU at a time. Therefore, the pairs $\{S_g^1, S_g^2\}$ are complementary, each pair corresponding to a single decision. We thus introduce a switch decision vector $\mathbf{s} = [S_1^1\, S_2^1\, \ldots\, S_{n_P}^1\, S_X^1]$. The set $\mathcal{R}$ contains all the 2^{n_P+1} possible switch combinations, each represented by a unique $\mathbf{r}$. The operational algorithm follows these steps:

1. Retrieve desired load schedule, solar generation forecast, SoC of each battery, and fault location, if a fault is detected. These are the algorithm inputs.

2. Calculate battery energy availability (during eclipse).

3. Modify constraints to reflect the status of the system (normal/fault), as mentioned in Table 4.1.

4. Modify line power flow constraints to reflect the considered switch combination $\mathbf{r}$.

5. If $S_X^1 = S_X^2 = 1$, modify reference node voltage constraint to set only one MBSU node voltage equal to V_{nom}, with $m_1 \in \mathcal{M}$ being the default node.

6. Solve the optimization problem and store the maximum objective function value (f) for all allowable switch decision combinations ($\mathcal{R}_a \subseteq \mathcal{R}$), repeating steps 4 and 5 each time. This constitutes the outer loop of the algorithm.

Table 4.2. Maximum PDU power demands and network parameters

Maximum power demand		Cable resistances		
PDU no.	$P_{D,\max}$ (kW)	From node	to node	value (mΩ)
1	2.8	1	4	4.0
2	2.3	2	4	3.2
3	2.6	3	4	4.0
4	2.7	5	4	4.0
5	2.8	7	4	6.0
6	2.6	9	4	8.0
7	2.4	11	4	10.0
8	2.7			

7. If the highest magnitude of f is attained in more than one combination, choose the one which leads to the least network energy loss, estimated by

$$\frac{\Delta t}{2} \sum_{k=k_1}^{k_T} \sum_{s=1}^{n_N} \sum_{\substack{r=1 \\ r \neq s}}^{n_N} G_{s,r} (V_{s,k} - V_{r,k})^2 \,. \tag{4.23}$$

To visualize the solution, we define three indices related to the load power as follows. Let all loads at time k belong to $\mathcal{L}_{v,k}$, $\mathcal{L}_{s,k}$, and $\mathcal{L}_{n,k}$, if they are considered to be vital, semi–vital, and non–vital, respectively. The index $H_{v,k}$ is defined as the ratio of the sum of decision variables ($b^g_{h,k}$ or $c^g_{h,k}$) of loads in $\mathcal{L}_{v,k}$ to the total number of loads in $\mathcal{L}_{v,k}$. The indices $H_{s,k}$ and $H_{n,k}$ are similarly defined over the sets $\mathcal{L}_{s,k}$ and $\mathcal{L}_{n,k}$, respectively. Since the algorithm prioritizes vital loads over semi–vital loads, and semi–vital over non–vital loads, it is expected that $0 \leq H_{n,k} \leq H_{s,k} \leq H_{v,k} \leq 1$. Table 4.2 contains more information about the system in the case studies. The power consumption of individual loads at each PDU is 80–750 W. The OPF was solved for $\Delta t = 5$ minute intervals using Gurobi Optimizer. Each optimal solution was obtained within a few seconds. The complete system information, including power demand of each load and weight assignment at every interval, can be obtained from [53].

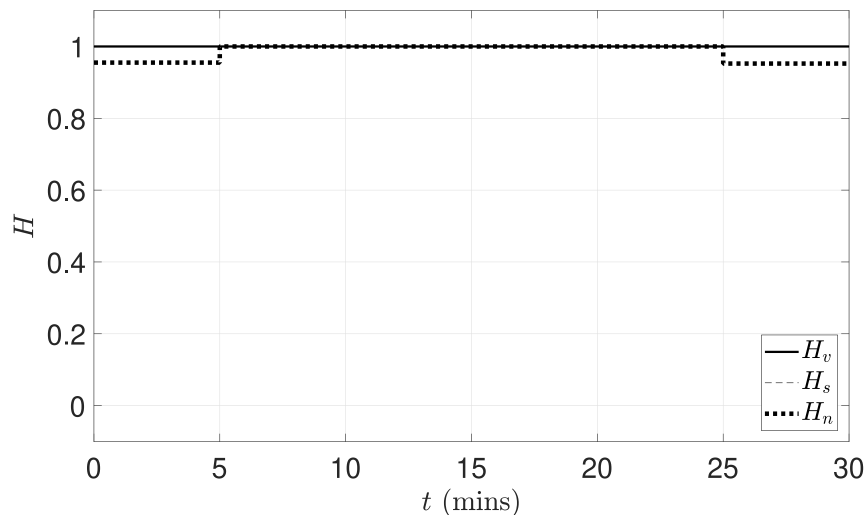

Figure 4.5. Load serving indices following BAT-2 malfunction.

4.3.1 Case study: normal operation

In this case study, we analyzed the OPF solution when the system was operating in normal condition. As mentioned in Table 4.1, only the configuration corresponding to $\mathbf{s} = [1\,1\,0\,0\,1\,1\,0\,0\,0]$ was evaluated. All load demands were met during insolation, even with the initial SoCs of all batteries set to $z_{\min} = 20\%$. Thus, $H_{v,k} = H_{s,k} = H_{n,k} = 1$, $\forall k \in \{k_1, \ldots, k_T\}$. The C-rate chosen by the algorithm for charging all batteries was 1C. All loads were also served during an eclipse, with $z_0 = 90\%$ for all batteries.

4.3.2 Case study: battery malfunction during eclipse

In this case study, a malfunction of BAT-2 occurring at the very beginning of an eclipse was considered, which led to its disconnection. With one less battery functional and $z_0 = 90\%$ for the remaining batteries, the algorithm decided that some non-vital loads had to be shed, as observed from Fig. 4.5. The optimal switch combination was determined to be $\mathbf{s} = [0\,1\,0\,0\,1\,1\,0\,0\,1]$. Only the MBSU-1 node voltage was regulated to V_{nom}, according to Step 5 of the algorithm. As an example, the PDU-3 power demand over time and the amount of power curtailment determined by the algorithm is shown in Fig. 4.6. Table 4.3 lists the PDU-3 load dispatch during the 0–5 min interval.

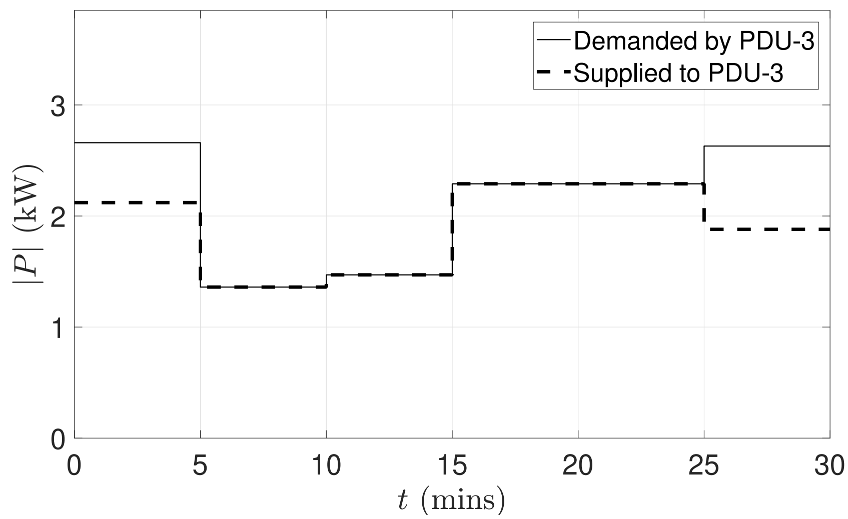

Figure 4.6. Power demand and supply of PDU-3 following BAT-2 malfunction.

Table 4.3. PDU-3 results during BAT-2 fault

Load no. (h)	Type	P^3_{Dh} (W)	W^3_h	decision (b^3_h or c^3_j)	
				normal	BAT-2 fault
1	binary	150	500	1	1
2	binary	750	1	1	1
3	binary	380	50	1	1
4	binary	80	50	1	1
5	continuous	750	1	1	0.28
6	continuous	180	50	1	1
7	continuous	260	1	1	1
8	continuous	110	500	1	1

4.3.3 Case study: solar array fault during insolation

A fault in SA-2 occurred at the very beginning of the insolation period, which led to its disconnection. Therefore, to charge BAT-3 and BAT-4, power from SA-1 had to flow through the cross-bus tie, as mentioned in the second row of Table 4.1. The initial SoCs of the batteries were 30%, 35%, 45%, and 25%, respectively. The algorithm selected switch combination $\mathbf{s} = [1\,1\,1\,1\,1\,1\,1\,1\,1]$, and the optimal C-rates as 0.8C, 0.7C, 0.6C, and 0.8C, respectively. The resultant power injections into the BCDU nodes are shown in Fig. 4.7. As seen from the plots, the battery SoCs reached 88.6%, 88.6%, 89.2%, and 87.9%, respectively,

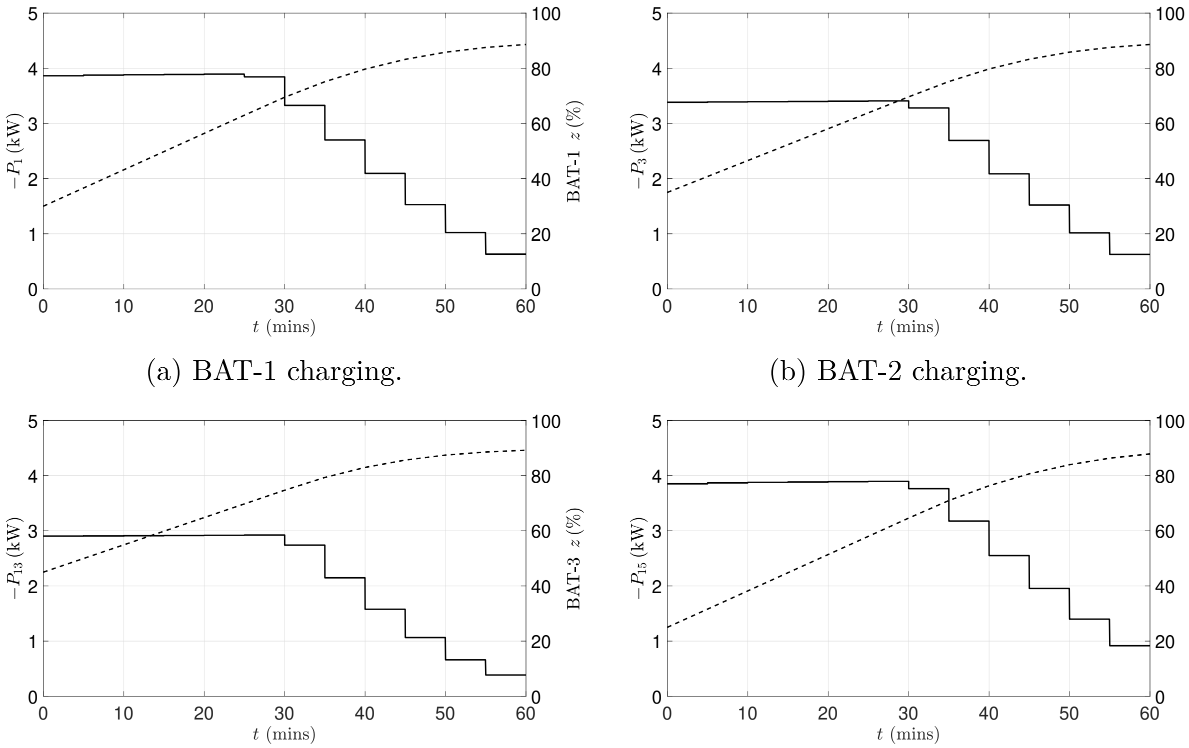

(a) BAT-1 charging.

(b) BAT-2 charging.

(c) BAT-3 charging.

(d) BAT-4 charging.

Figure 4.7. BCDU input power and battery SoC charging following SA-2 fault.

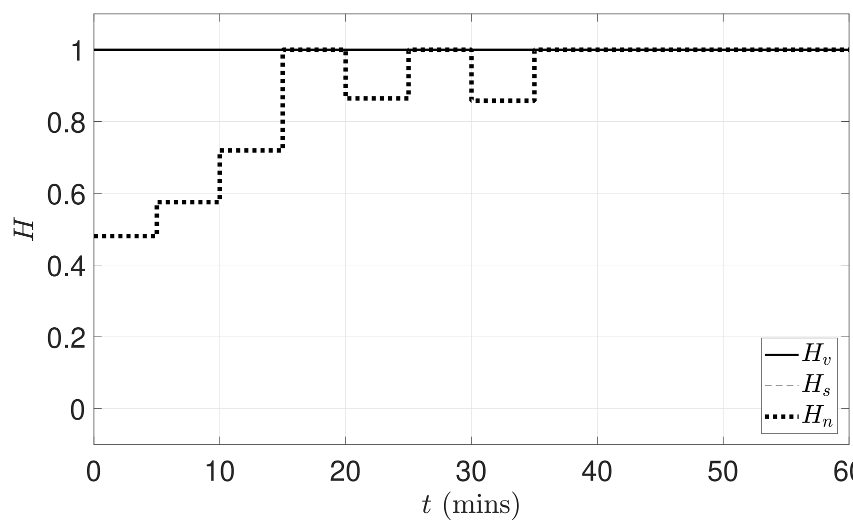

Figure 4.8. Load serving indices following SA-2 fault.

by the end of the insolation period. The plot in Fig. 4.8 implies that all vital and semi-vital load demands were fully met.

4.3.4 Case study: line short during eclipse

In this case study, at the beginning of the eclipse period, a line-to-ground fault occurring on line $l_{4,9}$ was considered. To clear the fault, the normally closed switch S_5^1 was opened. Hence, S_5^2 was closed to maintain power supply to PDU-5. It was assumed that all batteries had $z_0 = 85\%$ when the fault occurred. In this case, $\mathcal{R}_a$ contains all switch combinations with the fifth element of $\mathbf{s}$ fixed to zero. Solving the OPF for all these combinations (Step 6 of the algorithm), 177 switch combinations achieved the highest value of objective function, and were shortlisted. For all shortlisted combinations, $H_{v,k} = H_{s,k} = H_{n,k} = 1, \forall k \in \{k_1, \dots, k_T\}$, as observed from Fig. 4.9. Among these, the maximum energy loss was estimated as 28.28 Wh. The optimal switch combination determined by the algorithm in Step 7 was $\mathbf{s} = [1\,1\,0\,0\,0\,1\,0\,1\,0]$, because it led to the minimum network losses, approximately 16.84 Wh.

A simpler solution would have been to connect PDU-5 to MBSU-2, without checking all possible system configurations. The PDUs that remained connected to MBSU-1 (PDUs-1, 2, and 6) could then meet all their load demands. However, MBSU-2 would be connected to 5 PDUs, whose entire load demand would not be met due to the limited energy capacity of the batteries. The vital and semi-vital loads would have been unaffected but non-vital load index would have reduced as seen in Fig. 4.9.

4.3.5 Case study: simultaneous MBSU and battery fault during eclipse

At the very beginning of an eclipse, all batteries had been charged to 80% when BAT-4 developed a fault. As a result, some non-vital loads were shed, and $\mathbf{s} = [1\,1\,0\,0\,1\,1\,1\,0\,0]$ was selected for optimal system operation. Ten minutes later, another fault occurred at MBSU-1. As a result of this fault, SA-1, BAT-1, and BAT-2 were disconnected from the system. The algorithm was rerun under the additional conditions listed in row 5 of Table 4.1 to obtain a new solution until the end of the eclipse. Accordingly, all PDUs were connected to MBSU-2 via switches $S_g^2, \forall g \in \{1, \dots, n_P\}$, and only the MBSU-2 node voltage was regulated to V_{nom}. With BAT-3 acting as the sole power source, which had discharged to 65.34% at $t = 10$ minutes, all non-vital and semi-vital loads were shed, and even the vital

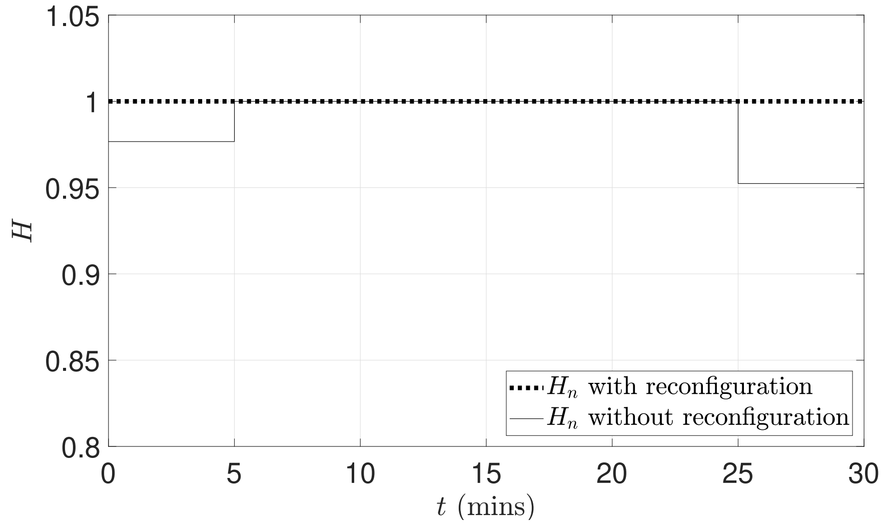

Figure 4.9. Non-vital load index following a fault in $l_{4,9}$.

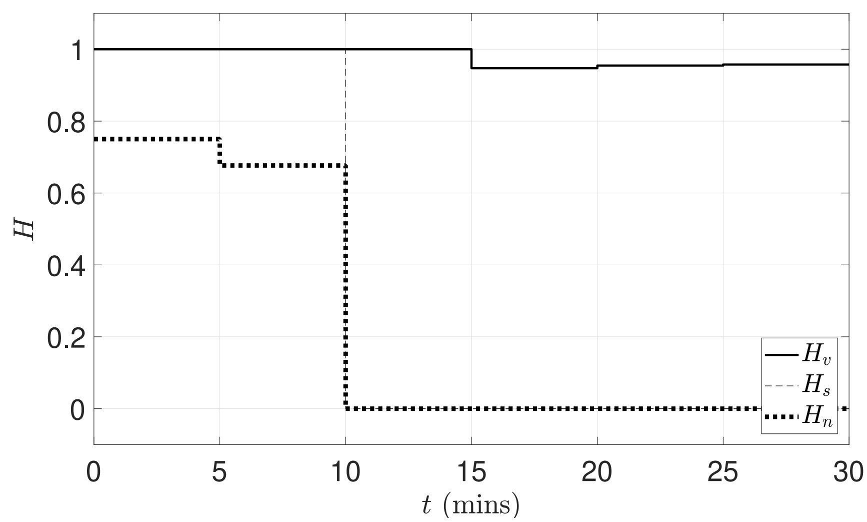

Figure 4.10. Load serving indices following MBSU-1 and BAT-4 faults.

load index $H_{v,k}$ dropped below 1 in some subsequent time intervals of the eclipse, as observed in Fig. 4.10.

5. CONCLUSION AND FUTURE WORK

The architecture and operation of a deep space vehicle (DSV) power system differs from the extensively studied terrestrial power system. Important differences lie in the way load is forecast, generation is scheduled, physical states are monitored, and the operational objectives. The power system of a DSV also needs to operate autonomously because of high latency in communicating with ground-based mission control. This work focuses on three aspects for achieving autonomous, fault-tolerant operation in the dc power system of a spacecraft.

First, utilizing the features of the distributed software agents [14] in the power system, we propose performing state estimation is performed locally for each unit (PDU or MBSU), based on Weighted Least Squares (WLS) estimation. The resultant WLS formulation can be simplified by making suitable approximations, which gives us insight into the effect of various measurements on the estimates. An important observation is that the current estimation can be treated as in independent problem, which can be followed by voltage estimation using simple arithmetic expressions. Using the resulting mathematical equations can speed up the computation without significant loss of accuracy.

The accuracy of estimates may suffer if any of the sensors develop a fault. In current sensor networks that have a low redundancy of measurements, a method to optimally select additional, practically realizable sensors is put forth. Including these additional sensors enables us to identify faulted sensors using the Largest Normalized Residual Test. A simple design for these sensors is also put forth, based on which the volume and weight penalty for the capability to identify faults is calculated.

Secondly, to identify component faults in the dc-dc power electronic converters in the system, a machine-learning based approach based on support vector machines (SVM), is suggested. Features related to the power-spectrum of the current signal are used to characterize different faults while training, and are used to classify them while testing the trained model. The algorithm is tested on waveforms generated by simulations of a dc-dc converter. The algorithm is able to return the system condition with high speed and reliability.

Future work can focus on hardware validation of the algorithms for identifying sensor and converter faults. Methods that inform the choice of features in SVM-based classification of converter fault classification can be explored.

Finally, an optimization algorithm is set forth that decides how to operate the power system under both normal and faulted conditions. The primary objective is ensuring service to important loads and fully charging the batteries, while a secondary objective is minimizing network ohmic loss. In the proposed algorithm, an OPF problem is formulated as a mixed integer linear program, and embedded inside an outer loop over all network configurations. The mathematical formulation is relatively simple and computationally efficient. Results of case studies considering various faults in the system show that the most critical loads are served by shedding unimportant loads and/or reconfiguring the network, and that batteries are charged in a way that maximizes their final state-of-charge.

In future work, a more detailed model of the batteries and converters can be included as part of the OPF problem. Minimizing the number of switching operations while reconfiguring the system can be another objective to be considered.

REFERENCES

[1] J. Soeder, A. McNelis, R. Beach, N. McNelis, T. Dever, L. Trase, and R. May, "Overview of intelligent power controller development for human deep space exploration," in *Proc. AIAA Propulsion and Energy Forum, 12th Int. Energy Conversion Engineering Conf. (IECEC)*, Cleveland, OH, Jul. 2014, ISBN: 978-1-62410-304-9. DOI: 10.2514/6.2014-3833.

[2] R. May, J. F. Soeder, R. Beach, P. George, J. D. Frank, M. Schwabacher, S. P. Colombano, L. Wang, and D. Lawler, "An architecture to enable autonomous control of a spacecraft," in *Proc. AIAA 12th Int. Energy Convers. Engin. Conf.*, Cleveland, OH, Jul. 2014, ISBN: 978-1-62410-304-9. DOI: 10.2514/6.2014-3834.

[3] P. Kulkarni, D. Aliprantis, B. Loop, and N. Wu, "Autonomous power dispatch for a deep space vehicle power system," in *Proc. IEEE Power and Energy Conf. Illinois (PECI)*, 2020, pp. 1–8.

[4] A. Primadianto and C. Lu, "A review on distribution system state estimation," *IEEE Trans. Power Syst.*, vol. 32, no. 5, pp. 3875–3883, 2017.

[5] M. Majdoub, J. Boukherouaa, B. Cheddadi, A. Belfqih, O. Sabri, and T. Haidi, "A review on distribution system state estimation techniques," in *Proc. 6th Int. Renewable and Sustain. Energy Conf. (IRSEC)*, 2018, pp. 1–6.

[6] M. Korkalı and A. Abur, "Detection, identification, and correction of bad sensor measurements for fault location," in *Proc. IEEE Power and Energy Soc. General Meeting*, 2012, pp. 1–6.

[7] A. Abur and A. G. Exposito, *Power System State Estimation: Theory and Implementation*. New York: Marcel Dekker, Inc, 2004.

[8] M. Meriem, C. Bouchra, B. Abdelaziz, S. O. B. Jamal, E. M. Faissal, and C. Nazha, "Study of state estimation using weighted-least-squares method," in *Proc. Int. Conf. Elect. Sci. and Technol. Maghreb (CISTEM)*, 2016, pp. 1–5.

[9] J. Zhao, M. Netto, and L. Mili, "A robust iterated extended kalman filter for power system dynamic state estimation," *IEEE Trans. Power Syst.*, vol. 32, no. 4, pp. 3205–3216, 2017.

[10] R. D. May, C. Beierle, Mingguo Hong, and K. A. Loparo, "Highly distributed state estimation for a dc spacecraft power system," in *Proc. IEEE Power and Energy Soc. General Meeting*, 2015, pp. 1–5.

[11] H. Tebianian and B. Jeyasurya, “Dynamic state estimation in power systems using kalman filters,” in *Proc. IEEE Elect. Power and Energy Conf.*, 2013, pp. 1–5.

[12] A. Alamin, H. M. Khalid, and J. C. Peng, “Power system state estimation based on iterative extended kalman filtering and bad data detection using normalized residual test,” in *Proc. IEEE Power and Energy Conf. Illinois (PECI)*, 2015, pp. 1–5.

[13] S. Yousefizadeh, J. D. Bendtsen, N. Vafamand, M. H. Khooban, F. Blaabjerg, and T. Dragičević, “Tracking control for a dc microgrid feeding uncertain loads in more electric aircraft: Adaptive backstepping approach,” *IEEE Trans. Ind. Electron.*, vol. 66, no. 7, pp. 5644–5652, 2019.

[14] R. May and K. Loparo, “The use of software agents for autonomous control of a dc space power system,” in *Proc. 12th Int. Energy Convers. Eng. Conf.*, Jul. 2014, ISBN: 978-1-62410-304-9. DOI: 10.2514/6.2014-3860.

[15] M. Wu and L. Xie, “Online detection of low-quality synchrophasor measurements: A data-driven approach,” *IEEE Trans. Power Syst.*, vol. 32, no. 4, pp. 2817–2827, 2017.

[16] L. Zhu and D. J. Hill, “Cost-effective bad synchrophasor data detection based on unsupervised time series data analytics,” *IEEE Internet of Things J.*, pp. 1–1, 2020.

[17] F. Aeiad, W. Gao, and J. Momoh, “Bad data detection for smart grid state estimation,” in *Proc. North Amer. Power Symp. (NAPS)*, 2016, pp. 1–6.

[18] R. J. Patton and J. Chen, “A review of parity space approaches to fault diagnosis,” in *Proc. IFAC Symp. Fault Detection, Supervision and Safety for Technical Processes*, 1991, pp. 65–81.

[19] H. Berriri, M. W. Naouar, and I. Slama-Belkhodja, “Easy and fast sensor fault detection and isolation algorithm for electrical drives,” *IEEE Trans. Power Electron.*, vol. 27, no. 2, pp. 490–499, 2012.

[20] M. Ben Hamed, L. Sbita, and S. Beni Hamed, “Direct current motor real time application of sensor and actuator faults detection and isolation based on structural residual space parity approach,” in *Proc. Int. Conf. Elect. Sci. and Technol. Maghreb (CISTEM)*, 2014, pp. 1–6.

[21] A. Viehweider, Kanghyun Nam, H. Fujimoto, and Y. Hori, “A fault detection and isolation scheme for lateral vehicle dynamics of EVs using a quantitative parity space approach,” in *Proc. 38th Annu. Conf. IEEE Ind. Electron. Soc.*, 2012, pp. 4630–4636.

[22] E. Balaban, A. Saxena, P. Bansal, K. F. Goebel, and S. Curran, “Modeling, detection, and disambiguation of sensor faults for aerospace applications,” *IEEE Sensors J.*, vol. 9, no. 12, pp. 1907–1917, 2009.

[23] S. Yang, A. Bryant, P. Mawby, D. Xiang, L. Ran, and P. Tavner, "An industry-based survey of reliability in power electronic converters," in *IEEE Energy Conversion Congress and Exposition (ECCE)*, Sep. 2009, pp. 3151–3157. DOI: 10.1109/ECCE.2009.5316356.

[24] F. Zidani, D. Diallo, M. E. H. Benbouzid, and R. Nait-Said, "A fuzzy-based approach for the diagnosis of fault modes in a voltage-fed PWM inverter induction motor drive," *IEEE Trans. Ind. Electron.*, vol. 55, no. 2, pp. 586–593, Feb. 2008, ISSN: 1557-9948. DOI: 10.1109/TIE.2007.911951.

[25] M. Beibei, S. Yanxia, W. Dinghui, and Z. Zhipu, "Three level inverter fault diagnosis using EMD and support vector machine approach," in *Proc. 12th IEEE Conf. on Industrial Electronics and Applications (ICIEA)*, Jun. 2017, pp. 1595–1598. DOI: 10.1109/ICIEA.2017.8283093.

[26] H. Lan, H. Liu, W. Yue, and N. Shen, "Intelligent fault diagnosis method in controlled rectifier based on support vector machines," in *Proc. Asia-Pacific Power and Energy Engineering Conf. (APPEEC)*, Mar. 2012, pp. 1–4. DOI: 10.1109/APPEEC.2012.6307674.

[27] M. A. Masrur, Z. Chen, and Y. Murphey, "Intelligent diagnosis of open and short circuit faults in electric drive inverters for real-time applications," *IET Power Electronics*, vol. 3, no. 2, pp. 279–291, Mar. 2010, ISSN: 1755-4535. DOI: 10.1049/iet-pel.2008.0362.

[28] N. V. Prasad Kuraku, Y. He, and M. Ali, "Probabilistic PCA-support vector machine based fault diagnosis of single phase 5-level cascaded H-bridge MLI," in *Proc. Int. Power Electronics Conf. (IPEC-Niigata 2018 -ECCE Asia)*, May 2018, pp. 2317–2323. DOI: 10.23919/IPEC.2018.8507478.

[29] J. Zhao, X. Gu, h. Yu, and Wangyan, "Fault diagnosis of power electronic based on multi-resolution analysis and support vector machine," in *Proc. Second Int. Conf. on Computational Intelligence and Natural Computing (CINC)*, vol. 1, Sep. 2010, pp. 121–124. DOI: 10.1109/CINC.2010.5643877.

[30] Z. Tian and X. Ge, "An on-line fault diagnostic method based on frequency-domain analysis for IGBTs in traction PWM rectifiers," in *Proc. IEEE 8th Int. Power Electronics and Motion Control Conf. (IPEMC-ECCE Asia)*, May 2016, pp. 3403–3407. DOI: 10.1109/IPEMC.2016.7512841.

[31] Y. M. Yeap, N. Geddada, K. Satpathi, and A. Ukil, "Time- and frequency-domain fault detection in a VSC-interfaced experimental dc test system," *IEEE Trans. Ind. Informat.*, vol. 14, no. 10, pp. 4353–4364, Oct. 2018, ISSN: 1941-0050. DOI: 10.1109/TII.2018.2796068.

[32] A. Ismail, L. Saidi, and M. Sayadi, "An open circuit switching fault diagnosis approach for back-to-back converter using wavelet analysis," in *10th International Renewable Energy Congress (IREC)*, Mar. 2019, pp. 1–6. DOI: 10.1109/IREC.2019.8754513.

[33] S. Khomfoi and L. M. Tolbert, "Fault diagnostic system for a multilevel inverter using a neural network," *IEEE Trans. Power Electron.*, vol. 22, no. 3, pp. 1062–1069, May 2007, ISSN: 1941-0107. DOI: 10.1109/TPEL.2007.897128.

[34] D. R. Espinoza-Trejo, E. Diez, E. Bárcenas, C. Verde, G. Espinosa-Pérez, and G. Bossio, "Model-based fault detection and isolation in a MPPT boost converter for photovoltaic systems," in *Proc. 42nd Annual Conf. of the IEEE Industrial Electronics Society (IECON)*, Oct. 2016, pp. 2189–2194. DOI: 10.1109/IECON.2016.7793421.

[35] J. Poon, P. Jain, I. C. Konstantakopoulos, C. Spanos, S. K. Panda, and S. R. Sanders, "Model-based fault detection and identification for switching power converters," *IEEE Trans. Power Electron.*, vol. 32, no. 2, pp. 1419–1430, Feb. 2017, ISSN: 0885-8993. DOI: 10.1109/TPEL.2016.2541342.

[36] T. Morstyn, B. Hredzak, and V. G. Agelidis, "Dynamic optimal power flow for dc microgrids with distributed battery energy storage systems," in *Proc. IEEE Energy Convers. Congr. Expos. (ECCE)*, Sep. 2016, pp. 1–6. DOI: 10.1109/ECCE.2016.7855059.

[37] A. A. Zazou, J. Gaubert, E. Chevrier, E. Grolleau, P. Richard, and L. Bellatreche, "Distribution network reconfiguration problem for energy loss minimization with variable load," in *Proc. 42nd Ann. IEEE Ind. Electron. Soc. Conf. (IECON)*, Oct. 2016, pp. 3848–3853. DOI: 10.1109/IECON.2016.7793560.

[38] M. Carrion and J. M. Arroyo, "A computationally efficient mixed-integer linear formulation for the thermal unit commitment problem," *IEEE Trans. Power Syst.*, vol. 21, no. 3, pp. 1371–1378, Aug. 2006, ISSN: 1558-0679. DOI: 10.1109/TPWRS.2006.876672.

[39] K. W. Hedman, R. P. O'Neill, E. B. Fisher, and S. S. Oren, "Optimal transmission switching with contingency analysis," *IEEE Trans. Power Syst.*, vol. 24, no. 3, pp. 1577–1586, Aug. 2009. DOI: 10.1109/TPWRS.2009.2020530.

[40] S. Bose, S. Pal, C. Scoglio, B. Natarajan, S. Das, and N. Schulz, "Analysis of optimized reconfiguration of power system for electric ships," in *Proc. North Amer. Power Symp.*, Arlington, TX, Sep. 2010, pp. 1–7. DOI: 10.1109/NAPS.2010.5618967.

[41] F. Shariatzadeh, N. Kumar, and A. K. Srivastava, "Optimal control algorithms for reconfiguration of shipboard microgrid distribution system using intelligent techniques," *IEEE Trans. Ind Appl.*, vol. 53, no. 1, pp. 474–482, Jan. 2017. DOI: 10.1109/TIA.2016.2601558.

[42] J. A. Taylor, *Convex Optimization of Power Systems*. Cambridge University Press, 2015.

[43] J. R. Brauer, "Hall effect and magnetoresistive sensors," in *Magnetic Actuators and Sensors*. 2006, pp. 143–163. DOI: 10.1002/0471777714.ch10.

[44] Magnetics. (2017). "Ferrite catalog," Magnetics.

[45] (May 2012). "EQ-317L linear Hall IC datasheet," Asahi Kasei Microdevices Corporation (AKM).

[46] N. Deng, Y. Tian, and C. Zhang, *Support Vector Machines: Optimization Based Theory, Algorithms, and Extensions*. Dec. 2012, pp. 1–315, ISBN: 9780429110283. DOI: 10.1201/b14297.

[47] J. C. Platt, "Probabilistic outputs for support vector machines and comparisons to regularized likelihood methods," in *Advances in Large Margin Classifiers*, MIT Press, 1999, pp. 61–74.

[48] J. Csank, J. Soeder, J. Follo, M. Muscatello, Y. H. Hau, and M. Carbone, "An autonomous power controller for the NASA human deep space gateway," in *Proc. AIAA Int. Energy Convers. Engin. Conf.*, Cleveland, OH, Jul. 2018. DOI: 10.2514/6.2018-4634.

[49] (Jan. 2019). "26650 datasheet," Lithium Werks Inc.

[50] (Feb. 2013). "Cylindrical battery pack design, validation, and assembly guide cover," A123 Systems.

[51] G. L. Plett, *Battery Management Systems, Volume 1 - Battery Modeling*. Artech House, 2015.

[52] A. Al-Haj Hussein and I. Batarseh, "A review of charging algorithms for nickel and lithium battery chargers," *IEEE Trans. Veh. Technol.*, vol. 60, no. 3, pp. 830–838, Mar. 2011, ISSN: 1939-9359. DOI: 10.1109/TVT.2011.2106527.

[53] P. Kulkarni. (2019). "Notional deep space vehicle power system parameters," [Online]. Available: http://dx.doi.org/10.21227/r2ak-nd75.